NTNU

Norwegian University of
Science and Technology

Wet Gas Airfoil Analyses

Tarjei Thorrud Larsen

NTNU

Norges teknisk-
naturvitenskapelige universitet

Institutt for energi- og prosessteknikk

EPT-M-2011-64

MASTEROPPGAVE

for

Student Tarjei Larsen
Vår 2011

Analyse av våtgass strømning over skovlprofil

Wet Gas Airfoil Analyses

Bakgrunn

De fleste store felt i Nordsjøen er utbygd med tradisjonell teknologi. Fokus har i de senere år skiftet mot mindre og mer fjerntliggende felt med begrenset infrastruktur. Utvikling og drift av slike felt krever ny kostnadseffektiv teknologi. Et helt sentralt element her er havbunnsbasert brønnkompresjon for å frakte brønnstrømmen direkte til land, eller mer fjerntliggende prosesseringsanlegg offshore.

Teknologien kan i enkelte tilfelle eliminere behovet for offshore prosessanlegg, noe som kan gi en formidabel kostnadsreduksjon. De fleste leverandører av turbomaskiner satser derfor på utvikling av havbunnsbaserte våtgasskompressorer. Noen få prototype konsepter eksisterer og det foregår i dag utstrakt testing og validering av teknologien.

Ved NTNU bygges det opp ulike forsøksrigger for å dokumentere de grunnleggende mekanismene relatert til våtgass kompresjon. Formålet til en av riggene er å dokumentere ulike strømningsregimer over et skovlprofil.

Mål

Basert på litteratur og eksperimentelt arbeid i rigg er det et mål å tilrettelegge rigg, samt visualisere og analysere våtgass strømning over et vingeprofil. Forholdet innebærer tilrettelegging av modell for visualisering og analyse av strømningsregimet.

Oppgaven bearbeides ut fra følgende punkter:

1. Tilrettelegge og gjennomføre forsøk i strømningskanal for væskefilm/luft-strømning. Valgt visualiseringsteknikk fra prosjekt benyttes.

2. Gjennomføre eksperimentelle forsøk for å dokumentere strømningsregime ved ulike testbetingelser.

3. Validere CFD-modell mot relevante testresultater.

" _ "

Senest 14 dager etter utlevering av oppgaven skal kandidaten levere/sende instituttet en detaljert fremdrift- og eventuelt forsøksplan for oppgaven til evaluering og eventuelt diskusjon med faglig ansvarlig/veiledere. Detaljer ved eventuell utførelse av dataprogrammer skal avtales nærmere i samråd med faglig ansvarlig.

Besvarelsen redigeres mest mulig som en forskningsrapport med et sammendrag både på norsk og engelsk, konklusjon, litteraturliste, innholdsfortegnelse etc. Ved utarbeidelsen av teksten skal kandidaten legge vekt på å gjøre teksten oversiktlig og velskrevet. Med henblikk på lesning av besvarelsen er det viktig at de nødvendige henvisninger for korresponderende steder i tekst, tabeller og figurer anføres på begge steder. Ved bedømmelsen legges det stor vekt på at resultatene er grundig bearbeidet, at de oppstilles tabellarisk og/eller grafisk på en oversiktlig måte, og at de er diskutert utførlig.

Alle benyttede kilder, også muntlige opplysninger, skal oppgis på fullstendig måte. For tidsskrifter og bøker oppgis forfatter, tittel, årgang, sidetall og eventuelt figurnummer.
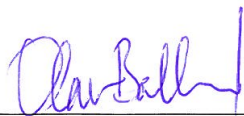
Det forutsettes at kandidaten tar initiativ til og holder nødvendig kontakt med faglærer og veileder(e). Kandidaten skal rette seg etter de reglementer og retningslinjer som gjelder ved alle (andre) fagmiljøer som kandidaten har kontakt med gjennom sin utførelse av oppgaven, samt etter eventuelle pålegg fra Institutt for energi- og prosessteknikk.

I henhold til "Utfyllende regler til studieforskriften for teknologistudiet/sivilingeniørstudiet" ved NTNU § 20, forbeholder instituttet seg retten til å benytte alle resultater og data til undervisnings- og forskningsformål, samt til fremtidige publikasjoner.

Ett -1 komplett eksemplar av originalbesvarelsen av oppgaven skal innleveres til samme adressat som den ble utlevert fra. Det skal medfølge et konsentrert sammendrag på maksimalt én maskinskrevet side med dobbel linjeavstand med forfatternavn og oppgavetittel for evt. referering i tidsskrifter).

Til Instituttet innleveres to - 2 komplette kopier av besvarelsen. Ytterligere kopier til eventuelle medveiledere/oppgavegivere skal avtales med, og eventuelt leveres direkte til de respektive. Til instituttet innleveres også en komplett kopi (inkl. konsentrerte sammendrag) på CD-ROM i Word-format eller tilsvarende.

NTNU, Institutt for energi- og prosessteknikk, 17. januar 2011

Olav Bolland
Instituttleder

Lars E Bakken
Faglig ansvarlig/veileder

Medveileder(e)
Ø. Hundseid, NTNU
T. Gruner, NTNU

Preface

This thesis finalize my Master of Science studies at NTNU, at the department of energy and process engineering.
To work with a subject this inspiring has been rewarding.

I would like to use the opportunity to thank some of the people who have been invaluable during this period.
My supervisor Lars E. Bakken for his excellent guidance, and making my last year a fun and memorable one. Joachim Mossige at Ansys help desk, for his patience and great tips on CFD. Staff engineer Erling Mikkelsen for his professionalism and for building my test channel. Last but not least, I will give an extra big thank you to my co-supervisors; PhD-candidate Trond G. Grüner and PhD Øyvind Hundseid, is has been challenging but fun to work with you. PhD Øyvind Hundseid deserves an extra gratitude for his guidance and patience throughout the construction and experimental period.

Tarjei Thorrud Larsen
Trondheim, June 20, 2011

Abstract

Subsea wet gas compression renders new possibilities for cost savings and en-
hanced gas recovery on existing gas wells. Technology like this opens to make
traditional offshore processing plants redundant. With new technology, follows
new challenges. Multiphase flows is regarded as a complex field of study, and in-
creased knowledge on the fundamental mechanisms regarding wet gas flow is of
paramount importance to the efficiency and stability of the wet gas compressor.

The scope of this work was to study liquid film flow in a diverging test-channel.
The channel was designed to resemble conditions found over an airfoil or diffuser
in a compressor, with emphasis on study the separation of the gas boundary
layer over the thin liquid film. Boundary layer separation is closely connected
to instabilities (surge) in compressors and is an important aspect to shed light
on.

Tools used was the CFD-software Ansys CFX 13.0. CFX was validated against
experimental work were high speed camera was used in terms of flow visualiza-
tion. In addition, two dynamic pressure sensors were used in the channel with
the subsequent FFT-analysis, to study the influence of thin liquid films in a
compression process, also related to instabilities.

The CFD software has proven to give promising results on multiphase flows.
From the CFD-simulations it was found a significant decrease in the shear stress
in the gas phase over the liquid film, compared to air over a solid, smooth sur-
face. This finding implies that the liquid film induces an increase in frictional
losses for the gas phase, which leads to increased susceptibility for the gas phase
to separate. The gas phase was, however, not found to separate with the given
conditions. Visual similarities to the CFD-simulations were found from the
high speed camera recordings. It was observed a clear void on the profile sec-
tion with a substantial decrease in velocity, which can be related to boundary
layer separation. These observations is supported by the smooth liquid film
structure in this region. The FFT analysis shows a decrease in amplitude on
the frequency spectra when increasing the liquid mass flow.

Abstract in Norwegian

Undervanns våtgasskompresjon åpner for nye muligheter med tanke på kostnadsbesparelser og økt utvinningsgrad på eksisterende gassfelt. Dette er teknologi som kan gjøre tradisjonelle off-shore prosesseringsanlegg overflødige. Med denne nye teknologien følger det mange utfordringer. Flerfase strømninger er et veldig komplekst fagfelt, og økt førståelse av de fundamentale mekanismene innen våtgass-strømninger har stor betydning for våtgasskompressorens virkningsgrad og stabilitet.

Formålet med denne oppgaven var å studere væskefilm-strømning i en divergerende forsøkskanal. Kanalen ble designet for å etterligne forholdene man finner over et skovlprofil eller diffusor i en kompressor, med vektleggelse på å studere separasjon av gassgrensesjiktet over en tynn væskefilm. Separasjon av grensesjikt er tett koblet til ustabiliteter (surge) i kompressorer og er derfor et meget viktig aspekt å belyse.

Verktøyene som ble brukt var CFD-programvaren Ansys CFX 13.0. CFX ble å validert opp mot eksperimentelt arbeid der høyhastighetskamera ble benyttet for visualisere strømningen. I tillegg er det benyttet to dynamiske trykksensorer med påfølgende FFT-analyse i kanalen for å studere tynne væskefilmers innvirkning i en kompresjonsprosess, som også er relatert til ustabiliteter.

CFD-programvaren viste seg å ha lovende egenskaper på flerfasestrømninger. Fra CFD-simuleringen ble det funnet en stor reduksjon i skjærkrefter i luftfasen over væskefilmen, sammelignet med luft over en fast, glatt flate. Dette impliserer at væskefilmen induserer økte friksjonstap for gass-strømningen, som medfører økt sjanse for separasjon. Simuleringene konkluderte med at det ikke forekom separasjon med de gitte betingelser. Høyhastighetskameraet viste visuelle likheter med konturplot fra CFD-simuleringen. Det ble observert tydelige områder med lavere hastighet over den divergerende seksjonen som kan tenkes å være relatert til separasjon. Dette underbygges av observasjonen av glatt væskefilm-struktur i dette området. FFT-analysen viser en dempning av frekvensspekteret på væskefilmsiden når massestrømmen av vann økes.

Contents

Nomenclature

Roman symbols

$\dot{m}$	Mass flux	(kg/s)
$\dot{Q}$	Volume flux/flow	(m^3/s)
G	Mass flux per unit area	$(kg/s \cdot m^2)$
g	Gravitational constant	(m/s^2)
h_tot	Total enthalphy	(J/kg)
S_κ	Surface tension	(Pa)
u^*	Frictional velocity	(m/s)
u^+	Dimensionless velocity	(-)
U_{sg}	Superficial velocity, gas	(m/s)
U_{sl}	Superficial velocity, liquid	(m/s)
x	Quality	(-)
y^+	Dimensionless wall distance	(-)
$\mathbf{U}$	Velocity vector	(m/s)
A	Cross sectional area	(m^2)
B	Dimensionless constant	(-)
C	Droplet concentration	(-)
CFL	Courant Number	(-)
E	Entrainment fraction	(-)
k	Mass transfer coefficient	(-)
P	Wetted perimeter	(m)
p	Pressure	(Pa)
Re	Reynolds number	(-)
S	Source term in transport equation	(-)
T	Temperature	(K)
t	Time	(s)

Subscripts and superscripts

α	Indicating a phase	
g	Gas	(-)
l	Liquid	(-)
s	Superficial	(-)
el	Entrained droplets	(-)
h	Hydraulic diameter	(-)
hg	Hydraulic diameter on gas phase	(-)
hl	Hydraulic diameter on liquid phase	(-)
T	Transposed matrix	(-)

Greek symbols

α	Gas volume fraction	(-)
$\Delta\rho$	Density difference	(-)
Δt	Time step	(s)
Δx	Step size	(m)
$\dot{\epsilon}$	Entrainment rate	$(kg/m^2 s)$
$\dot{d}$	Deposition rate	$(kg/m^2 s)$
Γ	Diffusivity	$(\frac{kg}{m \cdot s})$
γ	Dimensionless constant	(-)
κ	Wavenumber	(1/m)
λ	Wavelength	(m)
μ	Viscosity	$(kg/s \times m)$
∇	Nabla operator	(-/m)
ν	Kinematic viscosity	(-)
∂	Partial derivative	(-)
ρ	Density	(kg/m^3)
τ	Stress tensor	(Pa)
θ	Refraction angle	(deg)
φ	Scalar quantity	(-)

ς	Shear strain rate	$(1/s)$

Abbreviations

CFD	Computational Fluid Dynamics	
e.g.	For example	
et. al.	And others	
fps	Frames per second	
GMF	Gas mass fraction	(-)
GVF	Gas volume fraction	(-)
i.e.	That is	
LDV	Laser Doppler Anemometry	
NACA	National Advisory Committee for Aeronautics	
PIV	Particle Image Velocimetry	
RANS	Reynold Averaged Navier-Stokes	
SST	Shear Stress Transport	
VOF	Volume of Fluid	

List of Figures

List of Tables

1 Introduction

The time has come when the possibility to find large gas reservoirs is almost gone. While there is a seemingly increasing emphasis on cost savings in the industry, the price for extracting oil and gas is increasing due to loss in well head pressure. This cost effective thinking has led to the rise of new applications focused on sub-sea technology. Sub-sea systems which can process and transport the product to shore or directly on to transport vessels without the need for large platforms and its crew.

Challenges lies in the fact that natural gas reservoirs contains a variety of components in different states. The need for processing this product has earlier been obvious. New technology on multiphase compressors has in the later years arose, which can handle the multi-component streams from the wells. Multiphase flows is regarded as highly complex field of study, and huge challenges arise to understand the interaction between the different phases.

The aim for this thesis is to study the flow regime in a stratified two-phase flow, in a diverging channel designed by the author. The emphasis will lie on the study of boundary layer separation of the gas phase over a thin wavy liquid film. Tools used will be the commercial CFD tool Ansys CFX which will be validated against experimental findings, using high speed photography and dynamic pressure sensors.

The report starts with an introduction to CFD and its capability on multiphase flows. Further, the fundamental concepts of multi-phase flows with emphasis on the stratified and annular flow regimes, which is present in wet gas compression applications. A short introduction to frequency analysis is also given. Then, a thorough description of the CFD model and the experimental setup is presented. Results, discussion and advices on further work is presented as the last parts of this thesis.

2 Theory

This chapter is intended to serve as the basis for the methods and the needed insight for conducting the experiments and simulations in this thesis. The main emphasis will lie on the CFD simulations and multiphase phenomenons that are important to understand.

2.1 CFD - Computational Fluid Dynamics

All the simulations in this thesis are done with the commercial software package Ansys CFX 13.0, with the accompanying software for generating the geometry and mesh. All simulation were run on a Dell Studio laptop with 3GB RAM and 2Ghz Intel Core2Duo processor. The CFX solver is an implicit solver and uses the finite volume method, described in various litterature, e.g. Versteeg [1]. CFX uses a face centered scheme, i.e. all values are calculated at the center of a grid cell. This chapter is mostly based on documentation material from the Ansys CFX Documentation [2] and EDR, the Ansys help desk for Scandinavia, EDR [3], and will serve as an overview of the underlying theory, capabilities and limitations of the CFD software used in this thesis.

2.1.1 Geometry & mesh

The mesh is in many ways the key for a successful and trustworthy result. Emphasis on making it as good as possible, and to adapt the mesh to the problem is invaluable. To evaluate a mesh, the Courant-Friedrichs-Lewy condition (hereafter Courant number) is introduced as an important parameter to evaluate the relationship between the velocity, time step and grid spacing in a transient simulation. From [4] the Courant number is given by:

$$CFL = \frac{u \cdot \Delta t}{\Delta x} \qquad (2.1)$$

The ratio in equation 2.1 tells us how good the information in the computational domain is propagated. A high Courant number tells us that the time step is maybe too high and therefore the information get lost in some cells. Figure 2.1 shows an example with time step/grid size ratio of 2. The importance of the Courant number is different between a implicit and explicit solving method. Hence the implicit solving method used in Ansys CFX yields less importance to the Courant number, but is still an important parameter to evaluate [2]. Another important aspect regarding the Courant number is that the mesh spacing is almost never homogeneous over the entire domain, due to minimizing the computational efforts and the use of inflation layers. A too high Courant number can cause the solver to struggle reaching convergence.
Ansys Mesh is able to use algorithms to refine the mesh in regions with rapid change in geometry, e.g. curvature and narrow regions. Given the high speed in the domain and the introduction of one extra fluid, one can conclude that a high mesh resolution on the channel is required to get a stable solution.
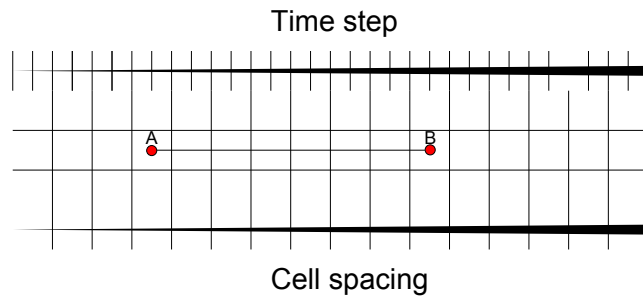
Figure 2.1: Illustration of the importance of the Courant number. As we move from point A to point B with $u = 1\,\text{m/s}$, $\Delta x = 1\,\text{m}$, and $\Delta t = 1\,\text{s}$ we get a Courant number of 2. Increasing the velocity or the time step will increase the Courant number, and fluid elements will make a "jump" over grid cells without giving any information about the flow in these cells.

Ansys Mesh gives the user the choice of multiple mesh types, which is useful for different applications. These types is divided into two types; structured and unstructured mesh. The type used in this thesis will be of a structured type consisting of hex-elements. This type is recommended for use in flow applications where there is strong gradients, which is the case for this diverging channel [3]. This type of mesh is illustrated in 2.2, also showing a typical inflation layer over the bottom of the channel. As figure 2.2 is illustrating, the mesh needs

(a) Mesh consisting of hex-elements.   **(b)** Hex-mesh in the near-wall region.
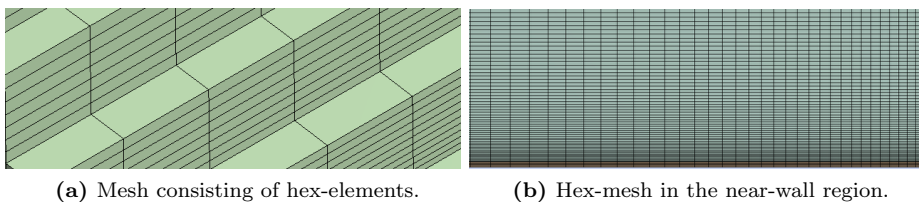
Figure 2.2: Illustration of hex-element mesh.

to heavily refined over the curved plate to capture any boundary layer separation. The refinement is also important to the turbulence model used. Different models treats low Reynolds number flow near a wall in different manner. For example the most validated model, the k-ϵ model is known to treat the near wall flow poorly, but is very good at a certain distance from the wall [2]. This implies that very high mesh resolution near the wall when using k-ϵ is a waste. This is considerations one have to have in mind when creating the mesh. As for this problem concerning boundary layer separation over the curved surface, a turbulence model capable of treating near-wall flow is essential.

2.1.2   Boundary conditions

According to the Ansys CFX Documentation [2] the choice of boundary conditions (hereafter BC's) is of great importance to the stability of the solution. The correct choice of BC's are of paramount importance to define the problem correctly.
In a channel with two inlets (water and air) and two outlets (water and air), the most robust constellation is regarded as velocity or mass flow at the inlet and static pressure at the outlet [5], [2]. For this simulation, the inlet condition is destined to be a velocity inlet since it is desirable to reproduce the velocity conditions from the laboratory experiments. With this constellation, the inlet total pressure becomes an implicit result of the configuration, and the problem is well posed.
For the condition at the outlet there is two alternatives. The Outlet type condition, and the Opening type boundary condition. The main difference between the two is that the opening type allows the flow reentering the domain, as illustrated by figure 2.3.

(a) The Outlet type BC not allowing flow to reentering the domain.

(b) The Opening type BC allowing the flow to reentering the domain.
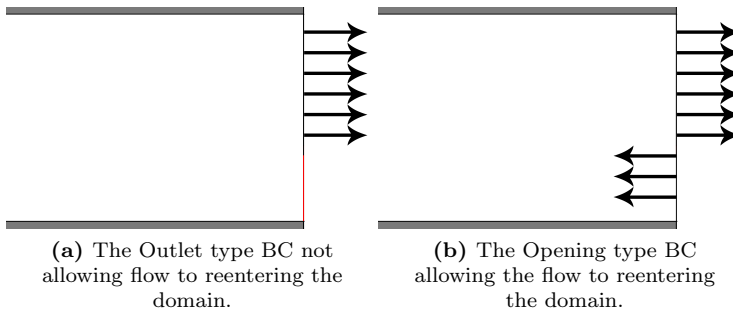
Figure 2.3: Difference between the two recommended outlet BC's

When an Outlet type is used, CFX does not allow flow reentering the domain and therefore it erects an artificial wall at the outlet to prevent this from happening. In cases were you have recirculating flows or separation bubbles in the near vicinity of the outlet, the solution is either to extend the domain so that it covers the whole recirculating region, or to switch to an opening type BC. If computational resources are readily available, the first alternative is the best and most stable [2]. For cases where you do not know the flow pattern at the outlet or that the model investigated sets restrictions to the domain geometry, one should use Opening. Both alternatives gives the opportunity to set a pressure level at the outlet. For the Outlet case, the most robust setting is a relative static pressure. For the Opening type, the CFX solver treats the pressure as relative static pressure if outflow, and relative total pressure if back flow. Due to the limited computational resources during this thesis, it is evident that the safest BC choice at the outlet is of an Opening type.

During the initial phase of this thesis, the Outlet alternative was tested and proven to create large numerical instabilities on this model.

2.1.3   Initial conditions

To make sure the solver is "on track" it is normal to specify a set of initial conditions for transient simulations. For simulations that are struggling to converge, correct specified initial conditions can often be the solution. The CFX solver offers a variety of different settings to the initial conditions. The most common and the default setting is to specify the velocity components in the domain when a velocity inlet is set as the inlet BC, together with turbulence intensity and a reference pressure. Another common approach is to run a steady state simulation till it reaches an accepted convergence level and then use these values as an initial condition. The latter is maybe the safest way since the former approach requires a good understanding of the flow pattern, and is therefore subjected to uncertainties.

2.1.4   Governing equations

As mentioned earlier the code in CFX 13.0 uses a Finite Volume Method (FVM). CFX solves the unsteady Navier-Stokes equation in their conservation form. The continuity equation is given by [2]:

$$\frac{\partial \rho}{\partial t} + \nabla \cdot (\rho \mathbf{U}) = 0 \tag{2.2}$$

The momentum equation:

$$\frac{(\rho \mathbf{U})}{\partial t} + \nabla (\rho \mathbf{U} \otimes \mathbf{U}) = -\nabla p + \nabla \cdot \tau + \mathbf{S}_M \tag{2.3}$$

Where τ is the stress tensor and is given by:

$$\tau = \mu \left(\nabla \mathbf{U} + (\nabla \mathbf{U})^T - \frac{2}{3} \delta \nabla \cdot \mathbf{U} \right) \tag{2.4}$$

And the total energy equation:

$$\frac{\partial (\rho h_{tot})}{\partial t} - \frac{\partial p}{\partial t} \nabla \cdot (\rho \mathbf{U} h_{tot}) = \nabla \cdot (\lambda \nabla T) + \nabla \cdot (\mathbf{U} \cdot \tau) + \mathbf{U} \cdot \mathbf{S}_M + \mathbf{S}_E \tag{2.5}$$

Where h_{tot} is the total enthalpy, which is defined as the static enthalpy plus the mechanical energy.
A version of these equations is also given in [6] and is only reproduced here to serve as an enlightenment to the governing equations for CFD-solvers.

2.1.5 Turbulence modeling

Accurate turbulence modeling is important concerning boundary layer problems like this. The choice of turbulence model can give solutions that differs a lot. The turbulence models that are most relevant here are the Reynolds Averaged Navier-Stokes - models (RANS), due to the computational limitations for the writer. The equations for these types of models are thoroughly shown in [6] and not reproduced here. The most promising model for near wall treatment is the k-ω SST, which was also used in the present authors project thesis [6].

2.1.6 Multiphase modeling

The multiphase possibility for stratified flow in CFX consists of the inhomogeneous and homogeneous free surface flow alternatives. The homogeneous model treats the whole flow field as one component. This applies to for example the pressure, velocity and turbulence equations. That is, the flow fields is shared, except for the volume fractions. This differs from the inhomogeneous model that solves the transport equations for each phase, and model the interaction between them. This implies that the inhomogeneous alternative is more computationally expensive than the homogeneous alternative which is only solving one bulk transport equation. The bulk transport equation is given for a scalar quantity, φ as:

$$\underbrace{\frac{\partial}{\partial t}(\rho\varphi)}_{\text{Transient term}} + \underbrace{\nabla\cdot(\rho\mathbf{U}\varphi)}_{\text{Convection term}} - \underbrace{\nabla\cdot(\Gamma\nabla\varphi)}_{\text{Diffusion term}} = \underbrace{S}_{\text{Source term}} \qquad (2.6)$$

Although the homogeneous option in CFX is set by default to treat all quantities except the volume fraction with equation 2.6, it is possible to treat only for instance the velocity field with an inhomogeneous approach. A more thorough explanation of the notation in these equations is found in appendix A.

2.2   Multiphase flow

Multiphase flows is regarded as a complex, highly empirical field of study. It is easy to be struck by the numerous correlations and empirical relations. For this thesis, there will be focused on the stratified and annular flow regimes and its characteristics. The experiments will be focused on the stratified regime, to understand the influence thin wavy liquid films has on the compressor stability.

In wet gas compression the flow regime will be of a annular type. A annular regime in these applications typically consists of a thin stratified liquid layer at the walls with dispersed droplets in the gas core. The annular regime is illustrated in figure 2.4.
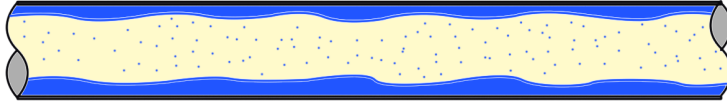
Figure 2.4: Illustration of a annular flow pattern.

2.2.1   Multiphase fundamentals

To characterize the velocity field in a stratified flow the superficial velocity is often used. From Schubring et. al. [7] superficial velocity is given for the gas and liquid phase respectively by:

$$U_{sg} = \frac{Gx}{\rho_g} \tag{2.7}$$

$$U_{sl} = \frac{G(1-x)}{\rho_l} \tag{2.8}$$

G is the mass flux per unit area:

$$G = \frac{\dot{m}_g + \dot{m}_l}{A} \tag{2.9}$$

x is the quality:

$$x = \frac{\dot{m}_g}{\dot{m}_g + \dot{m}_l} \tag{2.10}$$

And ρ_l and ρ_g is the densities for the two phases.

As always in fluid mechanics the Reynolds number plays an important role, and serves as an intuitively interpretation of the flow field. In a gas-liquid stratified flow the Reynolds number is given for each of the two phases. From Ng et. al. [8] the Reynolds number is given for the gas and liquid phase respectively:

$$Re_g = \frac{\rho_g U_{sg} D_{hg}}{\mu_g} \tag{2.11}$$

$$Re_l = \frac{\rho_l U_{sl} D_{hl}}{\mu_l} \tag{2.12}$$

Where D_h is the hydraulic diameter for gas and liquid. This is given by:

$$D_h = \frac{4A}{P} \tag{2.13}$$

A is the cross sectional area of the fluid and P is the wetted perimeter. It is normal practice to include the whole perimeter for the less viscous phase, and exclude the inter phase width for the more viscous one. Figure 2.5 illustrates this for a rectangular channel with a more viscous phase at the bottom.
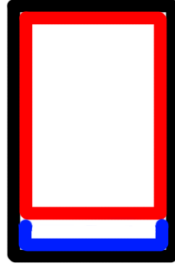
Figure 2.5: Illustration of the wetted perimeter in a cross section e.g. for a water-air system, since $\mu_{water} > \mu_{air}$. The red and blue lines are the perimeter for air and water respectively.

For wet gas flow, the Gas Volume Fraction (GVF) is defined as the gas volume flux divided by the total volume flux of the flow:

$$\alpha = \frac{\dot{Q}_g}{\dot{Q}_g + \dot{Q}_l} \tag{2.14}$$

Wet gas flow is defined as a multiphase flow containing up to 5 % liquids, i.e. from equation 2.14, $\alpha = 0.95$ [9]. Gas mass fraction is also used in wet gas analysis and is defined exactly as equiation 2.10.

2.2.2   Liquid entrainment

For high velocity concurrent flows the possibility of liquid entrainment is always present. Therefore the entrainment rate plays an important role regarding heat, mass and momentum transfer in annular flows. From Katoka et. al. [10] the entrainment rate is given by:

$$\dot{\epsilon} = \frac{D_h \rho_l U_{sg}}{4} \left(\frac{\partial E}{\partial z} \right) + \dot{d} \tag{2.15}$$

E is the entrainment fraction and $\dot{d}$ is the deposition rate. The entrainment ratio is simply:

$$E = \frac{\dot{m}_{el}}{\dot{m}_l} \tag{2.16}$$

Where the subscript el denotes entrained liquid. The droplet deposition rate can be approximated by:

$$\dot{d} \approx kC \tag{2.17}$$

Where k is the mass transfer coefficient and C is the droplet concentration in the gas core in the annulus. The deposition rate can be, according to Katoka et. al. [10] from the correlation by Paleev and Filipinovich be given more thoroughly as:

$$\frac{\dot{d}}{\rho_l U_{sl}} = 0.022 Re_g^{-0.25} \left(E\frac{U_{sl}}{U_{sg}} \right)^{0.74} \left(\frac{U_{sg}}{U_{sl}} \right) \left(\frac{\rho_g}{\rho_l} \right)$$

$$\tag{2.18}$$

$$\approx 0.022 Re_l^{-0.26} \left(\frac{\mu_g}{\mu_l} \right)^{0.26} E^{0.74}$$

Inserting this approximated correlation into equation 2.15 gives the complete entrainment rate:

$$\dot{\epsilon} = \frac{D_h \rho_l U_{sg}}{4} \left(\frac{\partial E}{\partial z} \right) + 0.022 \rho_l U_{sl} Re_l^{-0.26} \left(\frac{\mu_g}{\mu_l} \right)^{0.26} E^{0.74} \tag{2.19}$$

2.2.3 Interfacial waves

When the liquid film is subjected to a fast flowing concurrent gas-phase, there will be interfacial transfer of momentum, heat and mass between the two phases. In the case with no entrainment there will mainly be transfer of momentum if assuming the two phases are in thermal equilibrium. The momentum transfer will create wavy patterns at the liquid surface due to frictional forces. The form of the waves are highly dependent on the relative velocity between the two phases and the fluid properties. Since disturbed liquid films is known to impose increased frictional forces at the fluid interface [11], it is an important aspect regarding boundary layer separation that will be discussed in chapter 2.2.5 and 2.2.6.

Important parameters when considering interfacial waves is the wave height, the wave speed and the wave frequency. In addition, considerations regarding coherency is also important. The interface will typically go through five different regimes when the the gas superficial velocity is increased. These regimes are described by Hewitt [11] and is also given in the former project thesis by the author [6]:

Smooth surface   Occurring at low relative velocity between the gas and liquid phase.

Two-dimensional waves   Increasing the gas velocity causing the formation of small ripples. These ripples forms quickly two-dimensional low amplitude waves.

Three-dimensional waves   The latter regime evolves into a three-dimensional structure. The wave length and velocity is nearly the same as the two-dimensional case.

Roll waves   Larger roll waves appear as the gas velocity is further increased. These waves have approximately the double speed of the two and three-dimensional waves.

Atomization   Finally the wave crests will not sustain the high shear from the fast-flowing gas phase and will entrain from the surface. This phenomena is related to instability of liquid films, and is discussed in chapter 2.2.4.

2.2.4   Stability of liquid films

Due to high relative gas velocity in this experiment there will most certainly be entrainment of droplets into the flow. Entrainment can also be enhanced because of manufacturing imperfection. But isolated the stability of the liquid film is dependent mainly on the gas velocity and fluid properties. Most literature concerning entrainment and stability are related to annular flow regimes, which is present in a real compression process. The flux of moment and mass between the two phases are important aspects to understand and investigate, to be able to understand mechanisms at a boundary layer level.
Instability of stratified flows that figure 2.6 shows involves at least two of the following three mechanisms from Brennen [12]:
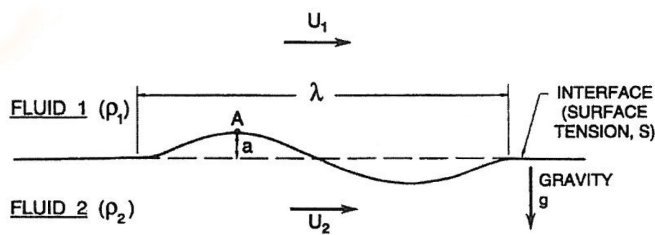
Figure 2.6: Schematic representation of the case of stratified wavy flow. From Brennen [12].

Buoyancy forces   In a stratified flow, the fluids will separate due to difference in density. This force can be both stabilizing and destabilizing, but in the case with water underneath air, this force is always stabilizing.

Surface tension force   Surface tension is always a stabilizing force at the interface between two fluids.

Bernoulli effect   Bernoulli effect is a change in the pressure along the interface. This effect is caused by the geometry of the wavy interface which changes the velocity of the gas phase, and therefore the local pressure. An increase in the gas velocity over a wave crest leads to a decrease in pressure, which in turn causes the wave crest to rise.

These three forces are known as the Kelvin Helmholtz instability. As a general rule the Kelvin Helmholtz instability is present when:

$$\underbrace{\frac{g\Delta\rho}{\kappa}}_{Buoyancy} + \underbrace{S_k}_{Surface\ tension} - \underbrace{\frac{\rho_g\rho_l\left(\Delta u\right)^2}{\rho_g + \rho_l}}_{Bernoulli\ effect} < 0 \tag{2.20}$$

As we can see from equation 2.20 the two first terms is always present, and the last term is therefore as mentioned earlier highly dependent on the relative velocity between the two phases ($\Delta u = u_1 - u_2$). The κ subscript is the wavenumber and is equal to $2\pi/\lambda$, where λ is the wavelength of the interfacial waves.

As the wave height a increases in a closed channel with height h, the gas flow in the channel experiences a slight perturbation in pressure which is opposed by buoyancy forces. This perturbation is given by a version of the Bernoulli equation:

$$p_A - \overline{p}_G = -\rho_G u_G^2 a/h \ \ for \ a << h \tag{2.21}$$

Where p_A is the reduced pressure and $\overline{p}_G$ is the reduction below mean gas pressure. The buoyancy effect is stabilizing to the Bernoulli effect and it follows that the flow is unstable when:

$$u_G^2 > gh\Delta\rho/\rho_G \tag{2.22}$$

Where the liquid velocity is assumed small compared to the gas and therefore neglected.

A short estimate for the channel herein shows that the flow will be unstable at the design speed of $U_g = 70m/s$ [6]. It is evident that the Kelvin Helmholtz instability plays an important role for onset of instability. For flows that is already unstable, some other mechanisms can however enhance this instability. For instance, Ishii et. al. [13] mention other mechanisms that can appear in a stratified flow pattern. These effects are illustrated in figure 2.7.

In figure 2.7 on the next page, the most likely mechanisms are the type one, and type four which will most likely occur in an annular flow. In many flows bubble formation occur in the liquid phase, either by boiling or simply by mixing of the two phases. This effect can not only lead to cavitation, but also degradation of the stability limit for the liquid film.
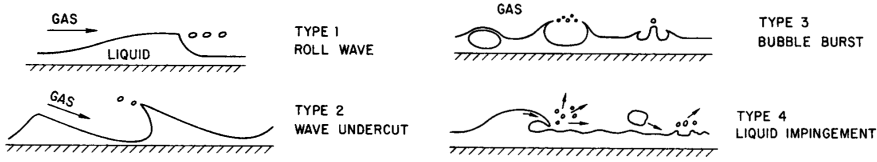
Figure 2.7: Illustration from Ishii et. al. [13] showing possible mechanisms for instability.

2.2.5   Friction factor correlations

The roughness of a surface has great importance to the flow over it. Well known correlations as the Moody [14] chart correlates the roughness of a material and the Reynolds number with a friction factor. The friction factor gives us the losses in the flow due to friction. Roughness is known to enhance the possibilities for boundary layer separation, due to the loss of energy caused by the rough wall on the flow. So the importance of roughness is prominent when considering flows in the near vicinity of a surface, solid or liquid.

As for solid surfaces, there is friction factor correlations for liquid surfaces. Most of the literature on the subject is heavily empirical based. The unpredictable nature of liquid waves creates a variety of different surfaces which in turn will give different values of the interfacial friction factor. Generally, the roughness imposed by a wavy liquid surface is larger than for solid surfaces. The problem of predicting frictional pressure drop is of paramount interest, both to further understand the whole flow field it selves and the energy transfer at the interface. The most known correlation for many years was the Lockhart and Martinelli correlation (1949), and is in many studies used as the standard of reference. The model consists of a set of parameters, which is normally plotted for design purposes. From Hewitt [11] the Lockhart - Martinelli parameters are given by:

$$\phi_G = \sqrt{\frac{\Delta P_{TP}}{\Delta P_G}} \tag{2.23}$$

and for liquid:

$$\phi_L = \sqrt{\frac{\Delta P_{TP}}{\Delta P_L}} \tag{2.24}$$

Where ΔP is the pressure gradient. Subscript TP denotes two-phase, and G and L denotes gas and liquid phase respectively. The last parameter in the model is given by the ratio between the liquid and gas pressure gradient:

$$X = \sqrt{\frac{\Delta P_L}{\Delta P_G}} \tag{2.25}$$

It is chosen not to derive these equations. A typical plot of equation 2.23, 2.24 and 2.25, from Hewitt [11] is shown in figure 2.8.
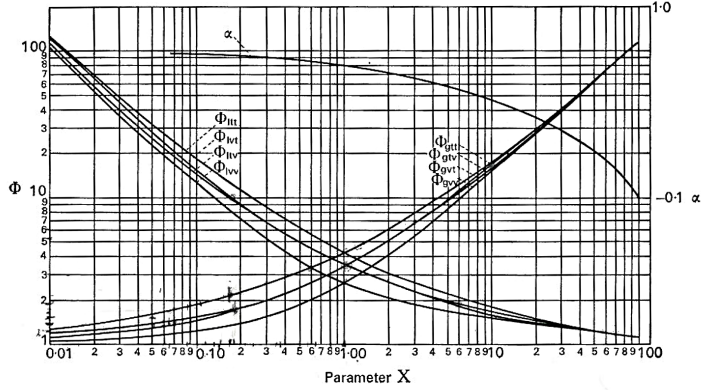
Figure 2.8: Representation of the Lockhart-Martinelli parameters. Subscript l and g denotes liquid and gas, whereas v and t denotes laminar and turbulent regime respectively. α on the right axis is the void fraction, i.e. $\alpha = 1$ if there is no liquid present.

Other correlations which dedicates to the friction factor alone is for example the proposition by E. T. Hurlburt and T. J. Hanratty [15]. This gives friction factor correlations for different flow regimes relative to a smooth surface:

$$\frac{f_i}{f_s} = 2 \quad \text{Smooth surface,} \quad (u_g - u_l) \leq (u_g - u_l)_{crit} \tag{2.26}$$

$$\frac{f_i}{f_s} = 5 \quad \text{Wavy surface,} \quad (u_g - u_l) \leq (u_g - u_l)_{crit} \tag{2.27}$$

$$\frac{f_i}{f_s} = 5 + 15 \left(\frac{h_L}{D} \right)^{0.5} \left[\frac{(u_g - u_l)}{(u_g - u_l)_{crit}} - 1 \right] \quad (u_g - u_l) \leq (u_g - u_l)_{crit} \tag{2.28}$$

Where subscript i and s denotes interface and surface respectively. h_L is the liquid height or holdup, and D is the pipe diameter. It is also stated that the ratio $\frac{f_i}{f_s}$ is a function of the wave height divided by the wavelength. Note that both equation 2.26 and 2.27 is considered to be in the stable region, i.e. the liquid surface is stable and no entrainment occurs, while equation 2.28 gives a correlation for friction factor above the critical relative velocity between the two phases. Equation 2.28 indicates that a thicker liquid layer (h_L) results in an increased interfacial friction factor. This corresponds well with the idea that a thicker liquid layer gives the possibility to large amplitude waves. Also Wallis(1969), reproduced in Belt et. al. [16], suggest that the interfacial friction factor is dependent on the film thickness and the pipe diameter in this early correlation which is analogous with full roughness. This correlation is given in means of the friction factor constant, C_f:

$$C_{f,i} = 0.0025 \left(1 + 300 \frac{\delta}{D} \right) \tag{2.29}$$

Here is $C_{f,i}$ the friction factor constant at the interface, δ the mean film thickness and D the pipe diameter. As for equation 2.28, equation 2.29 indicates that the friction factor is positively correlated with the mean film thickness.

2.2.6 Effects on the boundary layer

In turbo machinery applications one can regard the main flow as turbulent, although in some parts the boundary layer is laminar. Turbulent boundary layers are less susceptible to boundary layer separation due to the strong mixing by eddies in the near wall region, making inertia forces the prominent contribution in the boundary layer. This also implies that the velocity gradient is steeper for turbulent boundary layers. This is depicted in figure 2.9.
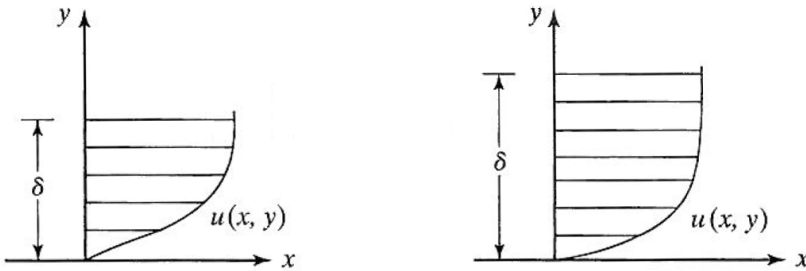
Figure 2.9: Illustration showing velocity profiles for a laminar boundary layer to the left, and the turbulent to the right. The turbulent is thicker than the laminar, denoted by δ. From [17].

The boundary layer thickness is defined as the distance from the wall where the velocity is 99% of the undisturbed flow. Fundamental boundary layer theory is presented in the former project thesis [6] and will not be reproduced here. The emphasis will lie on turbulent boundary layers and the influence of roughness.

Fundamental concepts for turbulent boundary layers share the same principles as for laminar, as they are base on the Navier-Stokes and the contiuity equation. The main difference is the Reynolds's time averaging of the continuity and momentum equations. The Reynold's time averaging is given by:

$$u = \overline{u} + u' \tag{2.30}$$

Equation 2.30 describes the velocity u with a mean component $\overline{u}$, and a fluctuating component u'. This relation yields also for other parameters. If equation 2.30 is inserted into the continuity equation and momentum equation the fluctuating component sums up to zero in every term, except from one which is the Reynolds stress term. This is the turbulent contribution to the total shear stress in the flow, and is typically much larger than the laminar shear contribution. Therefore, turbulent boundary layers is normally divided into regions

based on which forces that are dominating. This is known as the Logarithmic Overlap Law. From White [14] these are given as:

Wall layer   The layer close to the wall where the velocity is low, and viscous forces dominate.

Outer layer   Region where turbulent shear dominates the boundary layer.

Overlap layer   Layer in the middle of the two former where both types of shear are important. Figure 2.10 from White [14] illustrates the different layers.
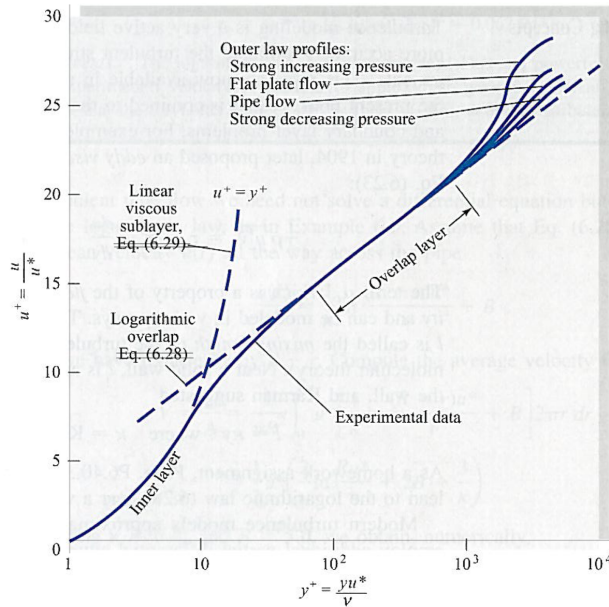
Figure 2.10: Illustration of the wall(inner), overlap and outer layer.

For convenience the equations which describes the different layers is in dimensionless form. For cosmetic reasons the Reynolds time averaged velocity $\overline{u}$ is denoted with u in the following expressions.
The wall layer is assumed linear and given by:

$$u^+ = \frac{u}{u^*} = y^+, \text{ where } u^* = \left(\frac{\tau_w}{\rho}\right)^{1/2} \tag{2.31}$$

The u^* is defined as the frictional velocity, although it is not a velocity but share the same units. τ_w is the wall shear. The parameter y^+ is the dimensionless distance from the wall, often used in boundary layer analysis and an important

parameter regarding mesh resolution in CFD computations. This parameter is defined in addition to in equation 2.31 by:

$$y^+ = \frac{yu^*}{\nu} \tag{2.32}$$

where ν is the kinematic viscosity and relates to dynamic viscosity by $\nu = \mu/\rho$. The wall layer is assumed to extend from $y^+ = 0$ to $y^+ = 5$. For the overlap layer the following equation yields:

$$\frac{u}{u^*} = \frac{1}{\gamma} \ln \frac{yu^*}{\nu} + B \tag{2.33}$$

where γ and B are dimensionless constants that varies in the literature. Later studies suggest a value of 0.41 and 5.0 respectively. The outer layer is given by:

$$\frac{U_e - u}{u^*} = -\frac{1}{\gamma} \ln \frac{y}{\delta} + A \tag{2.34}$$

where the nominator on the left hand side in equation 2.34 is known as the velocity defect, or the retardation of the flow due to wall effects. The constant A varies with the pressure gradient, and δ is the boundary layer thickness.

By looking at these equations it is evident that especially the wall layer and overlap layer is affected by the amount of wall shear. The wall shear is dependent on the roughness, and therefore the emphasis on the different regions in turbulent boundary layers is of great importance to study the separation effects over a thin wavy liquid film. And it is evident that an increase in the friction factor will lead to increased boundary layer momentum deficit. In Korgstad et. al. [18] and Aubertine et. al. [19] a modified version of equation 2.33 is introduced which takes into account the effect of roughness. This is given as:

$$\frac{u}{u^*} = \frac{1}{\gamma} \ln \frac{yu^*}{\nu} + B - \nabla \frac{u}{u^*} \tag{2.35}$$

where the last terms will act like a shift downwards for the velocity profile in figure 2.10 and is referred to as a roughness function. The shift can be seen on the plot from Krogstad et. al. [18] in figure 2.11 on the next page. Lost inertia in the boundary layer is therefore thought to make the boundary layer more receptive to the effect of an adverse pressure gradient, which is the prime source of boundary layer separation [20].
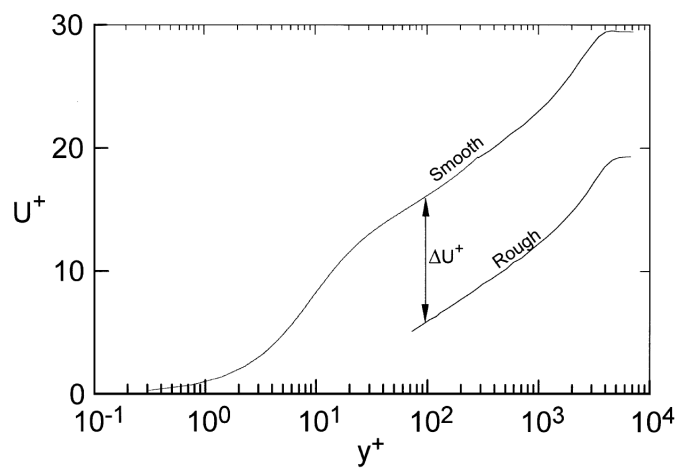
Figure 2.11: Illustration of the offset on the turbulent boundary layer profile when roughness is introduced. Where U^+ is equal to u/u^* and ∇U^+ equals the last term in equation 2.35.

2.3   Frequency analysis & instabilities

The motivation for this chapter is to further investigate the work of Trond G. Grüner et. al. [21] on compressors exposed to wet gas. The objective is to investigate and distinguish instabilities that are related to liquid film flow in a compressor.

2.3.1   Previous work

Instabilities in centrifugal compressors is caused mainly due to aerodynamical phenomenas. Operating range for a centrifugal compressor is limited by low flow conditions. After a certain decrease in flow the compressor will stall like on aircraft wings, the boundary layer over the blade or diffuser wall will separate causing pressure oscillations. At first stall occurs locally, and then evolve over the hole compressor if not stopped, a phenomena which is referred to as compressor surge. Surge can severely damage the compressor due to heavy vibrations. Stall is either desirable owing to loss in performance of the compressor. These phenomenas are well documented for dry-gas compressors, but not fully understood for compressors handling wet-gas. Grüner et. al. [21] experienced a stabilizing effect from the liquid when injected to a compressor at surge. Brenne [22] and Grüner et. al. [23] documented a premature separation in a diffuser and on an airfoil when exposed to liquid. These findings contradicts each other if one thinks instabilities is due to liquid presence, and emphasizing the complexity of multiphase flow in rotating machinery.

2.3.2   FFT - Fast Fourier Transform

This section is intended to give a short introduction to the concept of Fast Fourier Transforms.

A FFT analysis is a way of handling signals that are equally spaced. The FFT is derived from the Discrete Fourier Transform which is a approximation from the Fourier transform that is a well known mathematical application. The FFT is a lot faster algorithm than the DFT and is one of the most used signal processing techniques. The point of using FFT is to spot dominant frequencies from measured quantities in a system. The conventional Fourier transform of a function $f(t)$ is from [24]:

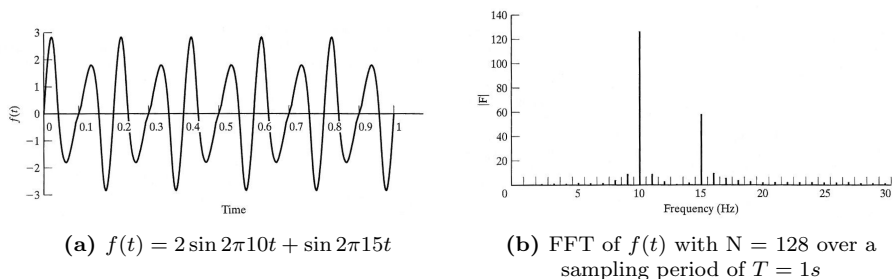$$F(\omega) = \int_{-\infty}^{\infty} f(t)e^{-j\omega t}dt \qquad (2.36)$$

The conventional Fourier transform is suitable in situations where you have a continuous function. In the case of data acquisition, the signals are stored at discrete time and the Discrete Fourier Transform is more applicable:

$$F(k\Delta f) = \sum_{n=0}^{N-1} f(n\Delta t)e^{-j(2\pi k\Delta f)(n\Delta t)} \quad k = 0,\ 1,\ 2, ...,\ N-1 \qquad (2.37)$$

Where N is the number of samples during the time period T. Equation 2.37 can be solved with numerical integration. The more computational cheap FFT model requires that N is a power of 2, i.e. $N = 128, 256, 512, ...$ To illustrate what happens when FFT is applied [24]: Given a function $f(t) = 2\sin 2\pi 10t + \sin 2\pi 15t$ which consists of two sine terms with frequencies $\omega = 10$Hz and $\omega = 15$Hz respectively. The function is plottet in 2.12a, the result from the FFT is illustrated in figure 2.12b.

**(a)** $f(t) = 2\sin 2\pi 10t + \sin 2\pi 15t$ **(b)** FFT of $f(t)$ with N = 128 over a sampling period of $T = 1s$

Figure 2.12: Illustration of the FFT method. *From [24].*

As figure 2.12 shows, peaks on $\omega = 10$Hz and $\omega = 15$Hz are dominant on the resulting FFT solution. Still, there is some smaller peaks visible, which is caused by the number of points used to discretize the signal (here, $N = 128$). Increasing the number of points will improve this filtering effect.

For the FFT analysis the LabView software from National Instruments is used. This is also the software used for monitoring and data sampling in the test facility. The software gives the opportunity to post-process and represent the data in a graphical manner.

The method of FFT is used by Trond G. Grüner [21] for predicting, and to recognize instabilities in a wet gas compressor. Figure 2.13 on the next page shows a waterfall graph from [21] where the compressor is run into instability by reducing the volume flow.

The goal for using FFT in this thesis is to compare two points in the channel, one point with and one without liquid interaction. These points is of equal distance from the inlet. For details see chapter 4.
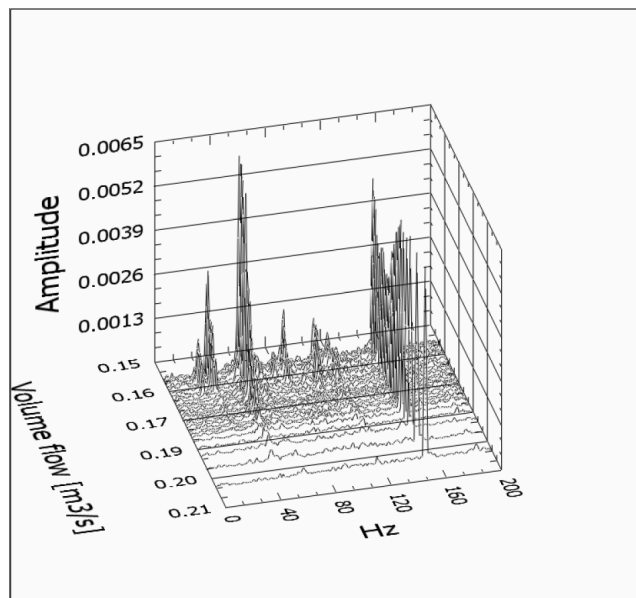
Figure 2.13: FFT-analysis showing peaks at lower amplitudes due to instabilities.
The larger peak at ≈ 150Hz is related to minor mechanical imbalances in the
compressor impeller.

3 CFD model

This chapter will give an overview of the characteristics of the CFD model used in this thesis.

3.1 Old CFD model

In the former project thesis by the present author [6] a two-dimesnional model of the channel was used for CFD-computations. The geometry and mesh was created using Gambit 2.4. For simulations, the commercial Ansys Fluent 12.0 package was used. Simulations to detect separation was performed, for both single -and two phase, with air and air/water as fluids, respectively. The Volume of Fluid (VOF) model [5] was used in the two-phase simulations. The 2D model was suitable to simulate the flow without any effects from the side walls. A 2D-model is less computational expensive, and was a good starting point for the investigation of boundary layer separation over a curved surface.

3.2 New CFD model

The motivation to create a 3D-model is first of all to make a better resemblance with the experiments in the laboratory. With the model in 3D it is expected to see the effect the walls have on the flow pattern. Even though the channel has a 2D-geometry it is anticipated that there will be some 3D effects, especially on the more viscous liquid layer. As mentioned in [6] there was also some aspects with the geometry that needed to be addressed to make the model more realistic, which is of great importance when comparing simulations with the laboratory experiment.
Another vital aspect with the 3D-model is that it is more expensive computationally than the simpler 2D-model. Computational time is of great importance, and to optimize between time used and the quality of the solution is therefore vital.

3.3 Geometry

The geometry is created using Ansys Design Modeler. To decrease the computational time, the model is halved at the inlet, i.e the model is 0.5 meter instead of 1 meter. This corresponds to a percentage decrease in total length of the channel by $\approx 30\%$. For details on the geometry, see chapter 4 and table 4.1. The remaining 0.5 meter of the inlet is needed in order to make sure the liquid film is properly developed. Complicated geometry, like the water injection nozzle is skipped for convenience when meshing the system. Instead, the water injection is made out of a rectangular portion of the channel inlet, and thus sharing the same inlet surface as for air. This simplification makes the mesh generation much easier, and good mesh quality easier to obtain. The height of the injection portion is 2 mm, and is shown in figure 3.1. The height of the water injection section is only a guess, as it is expected that the liquid film
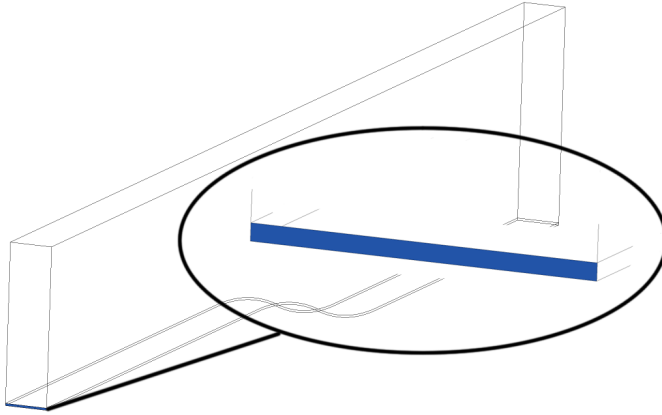
Figure 3.1: Illustration showing the simplified water injection module.

height will stabilize throughout the domain. In [6] this is also discussed. The
2 mm high portion of the inlet is cut through the whole domain. The cut is
parallel to the bottom surface of the channel, this is in order to make the mesh
sizing easier, and especially the inflation layer. The outlet section is in similar
manner as the inlet divided into two regions. This is because the Opening
type boundary condition discussed in chapter 2.1.2 require a volume fraction
of air and water set to each of the outlets of Opening type. This is discussed
further in chapter 3.5. The outlet section is also extended 0.1m compared to
the original model to prevent the development of a recirculating region at the
outlet boundary.

The rest of the channel reflects the channel geometry as dimensioned and built,
and is thus expected to provide a good basis for comparison.

3.4   Mesh

For easier computational efforts, the inlet domain is as mentioned above, half of
the length of the real geometry. This is strictly for increasing the computation
speed, and is not expected to have any significant effect on the solution in any
large degree. The flow at the inlet is always perpendicular and is assumed fully
developed at the region of interest. Further, it is chosen to use an inflation
layer from the bottom of the channel to capture the boundary layer and the
liquid film. The use of an inflation layer is because the liquid film requires a
high resolution mesh to emerge as a sharp interface in the final solution. It is
recommended that the liquid film is covered with at least five mesh elements
[25]. The fact that the mesh is refined near the floor of the channel, clearly will
increase the computational efforts together with the extra multiphase equa-
tions, but is needed to get acceptable results. To optimize the ratio between
computational time and number of elements in the domain, three meshes have

been made to investigate mesh dependencny. This is a part of the validation and verification process on the CFD model which is presented in chapter 5.

For these simulations it is chosen to use a method of meshing called Multi-zone. This method lets the user chose between different mesh types in different regions. In this case however, it is chosen to use hex-elements in the entire domain. Hex-elements is recommended, as mentioned in chapter 2.1 for flow conditions with strong gradients [3] and is the suitable choice here. Mesh resolution is controlled by setting the number of elements on the different parts of the model. The mesh resolution is set to increase towards the curved plate where boundary layer separation will appear, and decrease towards the outlet. This is illustrated in figure 3.2. As seen from figure 3.2, the edges of the mesh
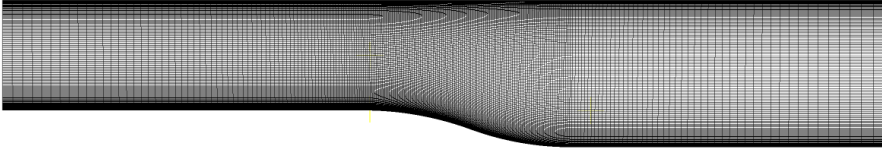
Figure 3.2: Mesh refinement.

is biased to get the increase of resolution towards the curved surface. Table 3.1 gives the number of elements on each of the edges used to control the mesh refinement. Number of elements and nodes are given in table 3.2. Regarding

Table 3.1: Refinement on used mesh

Edge	Physical size [mm]	Number of elements
Width of channel	40	5
Inlet water height	2	6
Inlet air height	148	133
Inlet section length	500	60
Profile section	270	88
Outlet section length	430	38

**Table 3.2:** Statistics on used mesh.

Elements	Nodes
129270	157080

the mesh quality, Ansys CFX Solver runs a check on the mesh before start-up. This mesh fulfills all criteria with good margins.

3.5   CFX setup

Due to the scope of this work and increased knowledge on the complexity of
multiphase flows, it is concluded to keep the simulations on a relative basic
level. This section will give an overview of the setup in Ansys CFX.

Ansys uses a work environment called Workbench for all their applications.
This is a "lobby" intended to give the user control over every step of the pro-
cess to set up a CFD - problem. A section of the user interface is shown in
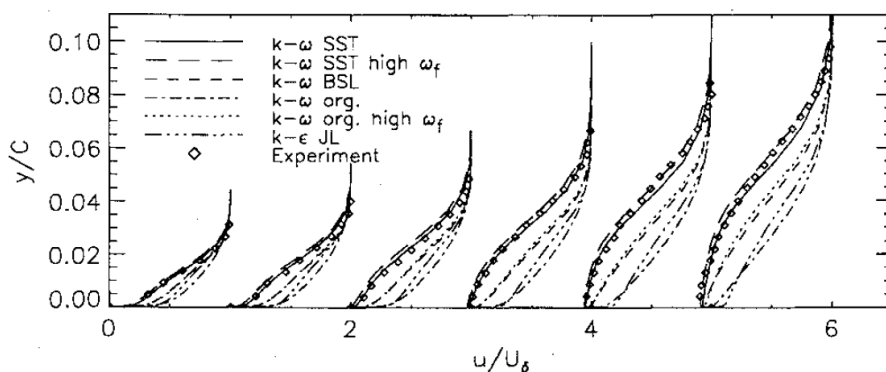figure 3.3.
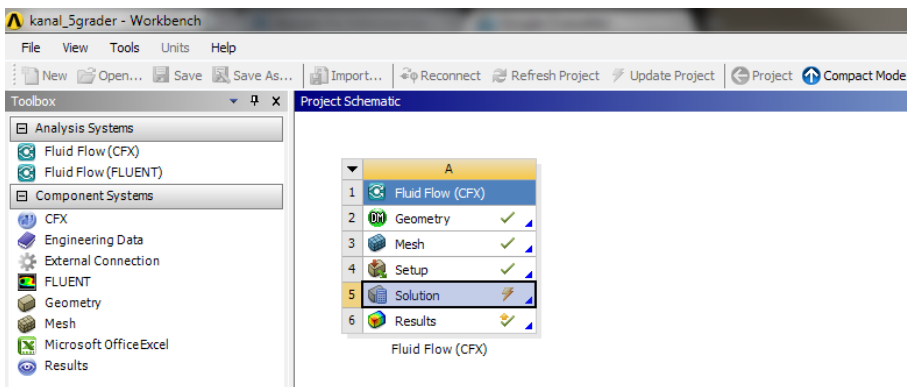
Figure 3.3: Workbench sets up a module (here CFX), with step-by-step setup
procedure for each of the elements in this module.

As figure 3.3 illustrates the first two steps are the geometry and mesh elements
which is already discussed in chapter 3.3 and 3.4.

3.5.1   Setup

Multiphase   The model is set up with the homogeneous free surface flow al-
ternative which is consistent with stratified flow, and shares similarities with
the VOF-model in Fluent [5]. The choice is based upon a compromise between
computational efforts and the level of results possible to obtain. The inhomoge-
neous alternative is a lot more computational expensive (discussed in chapter
2), and the results from this model is not believed to justify the extra time
spent at this point. As discussed in chapter 2, gravitation (buoyancy) is a sta-
bilizing force and is therefore included in the multiphase setup. The buoyancy
model is density based. Surface tension force is omitted due to large difficulties
reaching convergence, and is therefore thought to be the source of error.

Turbulence   As discussed in [6] and by recommendation from [3], the best suited RANS turbulence model is the k-ω SST. SST is a variant of the k-ω model with enhanced low Reynolds number treatment. The model is also suitable for flow over curved surfaces [25][26]. The backward facing step is a well known benchmark for turbulence models, and share a lot of similarities with this channel. Menter [26] evaluated several RANS models and concluded that the k-ω models, including SST performs better than other models on the backward facing step, and performs very well on aerodynamic applications compared to experimental results. Figure 3.4 shows the good behavior of the SST model on the suction side of an airfoil.

Figure 3.4: Velocity profiles on the suction side of a NACA4412 airfoil at 13.87 degrees angle of attack. From Menter [26].

This implies that the k-ω SST model is the correct choice for the geometry and flow conditions in this model. CFX uses in addition automatic wall functions if the mesh refinement is not sufficient. Buoyancy turbulence is disabled, since it will not give any contribution in these flow conditions.

Additional remarks   Multiphase in CFX offers a variety of different options. For these simulations the homogeneous free surface alternative is chosen for its simplicity and relatively cheap computational efforts. For the more comprehensive description of the problem setup it is referred to appendix F. In chapter 2.1.2 a discussion on the choice of boundary conditions is presented. Based on this, the velocity inlet type is therefore chosen also for the water inlet to provide stability to the solution.

4   Test facility

The tests were conducted at the Wet Gas Compressor facility at NTNU, in collaboration with the authors co-supervisors.

## 4.1   Construction

The main channel elements; walls, floor and roof are made out of 16 mm thick Plexiglas. The dimensions of the channel are given in the present autohors prosject thesis [6], and are here reproduced in table 4.1.

Table 4.1: Dimensions of the test channel

Part	H x W x L [mm]
Inlet section	150 x 40 x 1000
Diffusor & outlet section	200 x 40 x 600

The dimensions of the channel is discussed in [6], and is a result of a desired 2D-geometry and flow pattern. The channel is connected to a single stage, centrifugal wet gas compressor that is driving the flow. The compressors volume flow meter at that time was restricted to a max flow rate of air at $Q_{max} = 0.445\,\mathrm{m}^3/\mathrm{s}$, and therefore the max velocity in the channel is designed at this point with simple calculations performed in [6]. The experimental setup of the channel is shown in figure 4.1. For technical drawings of the channel and its vital parts, see appendix J.
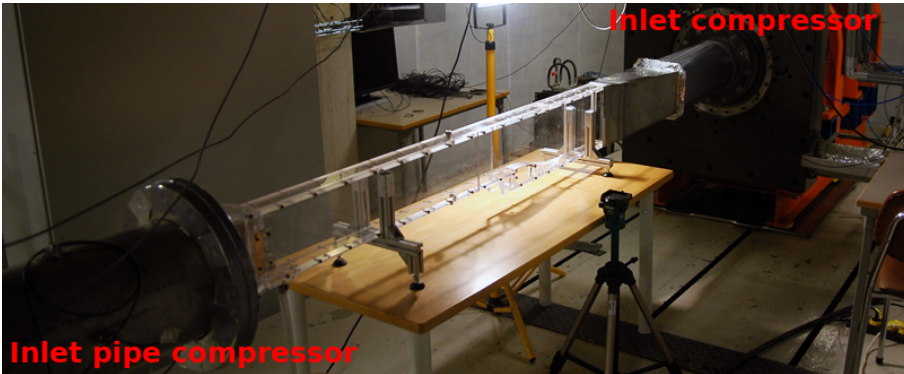

Figure 4.1: Experimental setup. The inlet piping with volume flow meter is connected at the inlet of the channel. The outlet of the channel is connected at the compressor inlet.

The channel is mounted between the inlet pipe of the compressor and the compressor inlet. At the inlet of the channel there is a transition-plate which merge the inlet pipe of the compressor with the channel. This is made out

of PVC, for drawings see appendix J. The outlet of the channel is connected to the compressor via a transition-duct, also illustrated in appendix J. In the transition-duct it is mounted a lattice between the two parts to prevent loose parts from damaging the compressor.

From the inlet of the channel and in towards the compressor inlet, there is 50mm to the water injection module. The module is made by an angled cut through the floor of the channel. At the water inlet, a hose flange is mounted to make connection easy. Water supply is provided by a pump capable of delivering water pressure up to 14 bar. For details on the injection module, it is referred to appendix J. Two Kistler dynamic pressure sensors (appendix E) is mounted 700mm from the inlet. One meter from the inlet, the channel starts to diverge. The diverging section consists of a curved profile with the possibility to adjust the angle of attack. For this channel there is manufactured three different bricks to be placed under the profile to set different angles of attack, and to make a smooth transition down to the channel floor. Different angles of attack is chosen to be 5, 10 and 15 degrees relative to the horizontal axis. An overview of the channel is shown in figure 4.2.
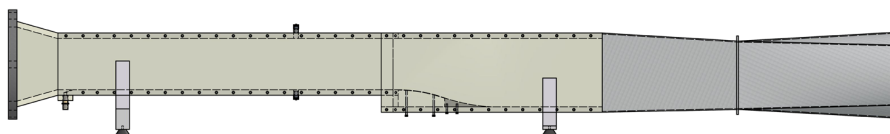
Figure 4.2: Schematic representation of the test-channel

4.2   Measurement techniques

Good measurement techniques for multiphase flows has always been challenging. Particular for this case were you want good measurements all the way down to the boundary layer over the liquid film. Figure 4.3 shows the intended measurement area on the channel.
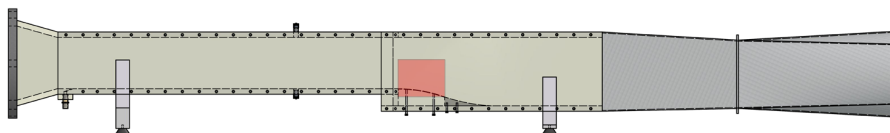

Figure 4.3: Main area of interest where the boundary layer separation takes place indicated by the red area.

In [6] several measurement techniques were discussed, and The PIV (Particle Image Velocimetry) method was chosen for its flexibility and ability to measure velocity over an area of interest. The LDV technique is an another technique considered, and is based on the same principles with particle seeding

in the phase of interest, but with the disadvantage of only measuring one point at a time.

Though both techniques where seemingly interesting for this experiment, both apparatuses are very dependent on the particle seeding to give accurate results [27]. A initial test with LDV together with the Swedish company VIDIX indicated large problems with laser techniques in multiphase flows. The test is documented in appendix B. In case of both LDV and PIV, measuring down to a boundary layer level, the wavy liquid film will most certainly "drown" the laser light, which subsequently will lead to inaccurate readings at boundary layer level. Secondly, at these high gas velocities, liquid entrainment will occur, liquid droplets will mix with the particle seeding in the gas phase which leads to great sources of error in the results. There exists different methods on the subject regarding digital object separation methods, for example from Honkanen et. al. [28]. These are mathematical methods that are applied to separate "good" particles from "bad". Methods like this are regarded as highly complex and would be a masters thesis on its own to study. Last, but utterly important, deposition of droplets on the channel walls will cause severe difficulties to the optical access of the system. At high gas velocities there will be droplet deposition on the channel wall, which in turn may form a thin liquid film. The wavy pattern of the liquid film will change the refraction angle of the laser light randomly as figure 4.4 is illustrating.
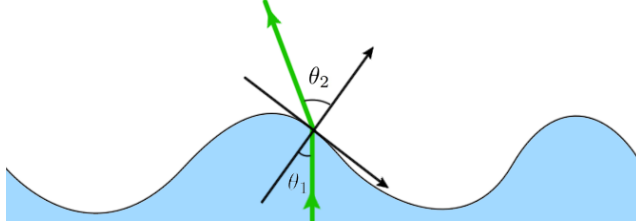
Figure 4.4: Illustration of the change in refraction angle caused by liquid waves.

This gained experience lead to dismissal of both the PIV and LDV techniques.

Instead high speed camera system for visualizing the flow was chosen. Visual observations provides good opportunities to understand and learn basic mechanisms, and is therefore thought to be a good starting point for the experiments at this point. A high speed camera is also versatile and easy to use, giving the opportunity to easily move the camera from one position to another without any major calibration.

4.3   Experimental setup and procedure

The primary objective of these experiments are to study separation of the gas phase boundary layer over a wavy liquid film. In addition dynamic pressure measurements on the floor (wet side) and on the roof (dry side) is conducted to study the effects of liquid film flow in a compressor, which can be related to previous work by Trond G. Gruner et. al. [21][23] concerning instabilities in wet gas compressors. Three parameters will be changed during the test; gas velocity, angle of attack and mass flow of water. The experiments will be executed with the test matrix shown in appendix H.

5   Results

This chapter will present the results obtained during this thesis. Results will briefly be discussed here, due to the visual nature of them. A summarized discussion will be presented in chapter 6. Comparison between CFD results and laboratory experiments regarding boundary layer separation over a thin wavy liquid film are studied.

5.1   CFD

All these results will concentrate on subjects discussed in chapter 2, that is the separation of the gas boundary layer over a thin liquid film subjected to an adverse pressure gradient. As an important part of the results, a section on the validation and verification of the CFD model is presented first.

5.1.1   Validation & verification

It is easy to blindly believe in the results that are presented from CFD simulations, and is often a pitfall. To make the choices regarding mesh and geometry more scientific correct, the validation and verification process is important when considering all numerical simulations [29]. In this case the simulations are transient, due to the transient phenomena separation. Because of the natural fluctuations in flow parameters in transient simulations, the use of control points in the domain will give confusing results when checking for mesh dependence. Therefore all the validation and verification processes will be conducted with steady state simulations. To optimize result values against computational efforts, three meshes with different resolution is made for the model with 10^0 angle of attack. Mesh statistics on these meshes is given in table 5.1. Ten

Table 5.1: Mesh statistics on the three tested meshes.

|	Coarse	Medium	Fine
Elements	90275	129270	162000
Nodes	109968	157080	196602

different monitor points is placed in the model domain. Three different parameters are evaluated; the pressure, superficial velocity of air and the difference in pressure ΔP between the outlet and inlet. The placement of these points are given in figure 5.1 on the next page. By looking at the parameter value in these points, one gets a qualitative idea on the quality of the different meshes. Except for the steady state option, the simulation setup is similar to the rest done in this thesis (described in chapter 3). It is chosen to set the inlet velocities to $U_{inlet-air} =$50 m/s and $U_{inlet-water} = 10$ m/s. Plots of this grid dependency test is shown in figure 5.2 and 5.3.
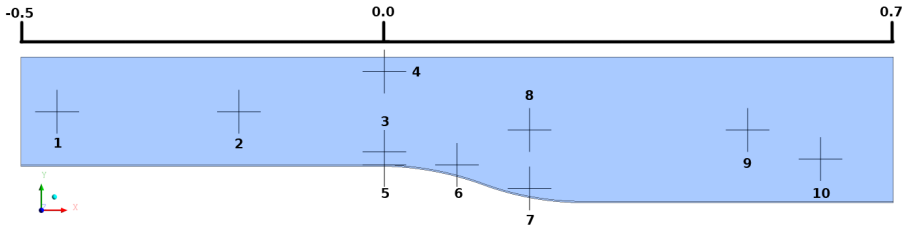
Figure 5.1: Cartesian coordinates for points: (1): (-0.45, 0.075, 0.02), (2): (-0.2, 0.075, 0.02), (3): (0, 0.02, 0.02), (4): (0, 0.13, 0.02), (5): (0, 0.002, 0.02), (6): (0.1, 0.002, 0.02), (7): (0.2, -0.03, 0.02), (8): (0.2, 0.05, 0.02), (9): (0.5, 0.05, 0.02), (10): (0.6, 0.01, 0.02)
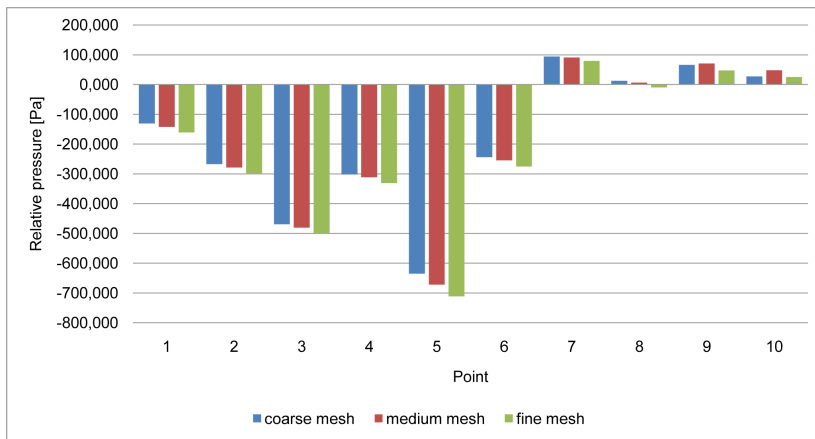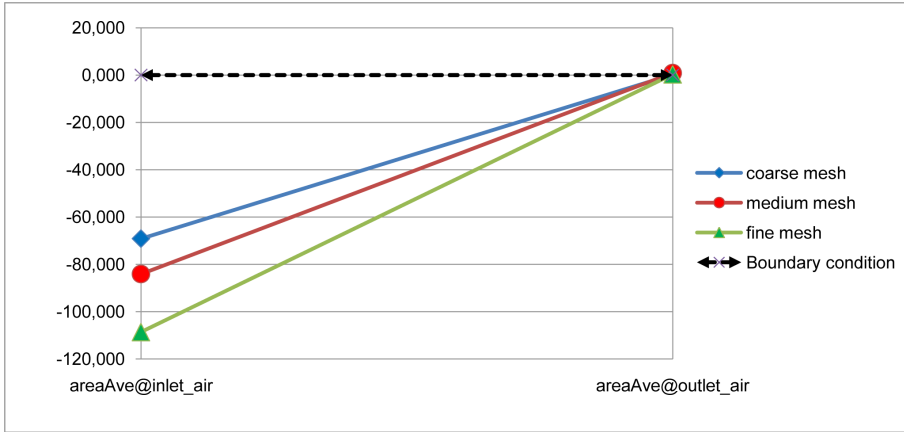

(a) Relative pressure
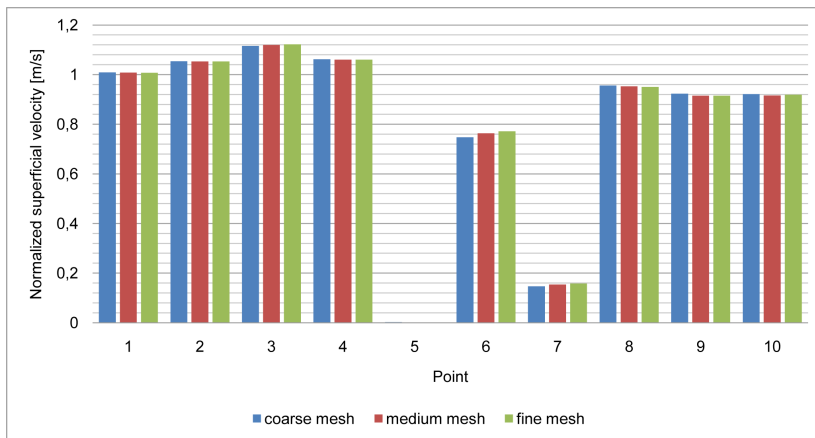
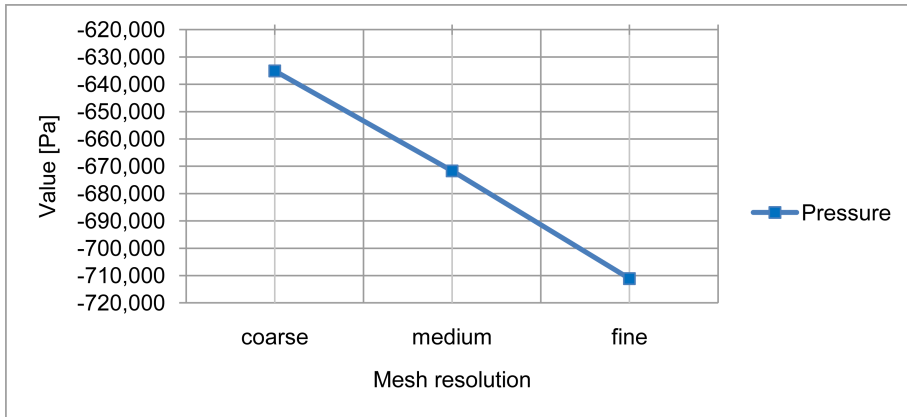**(b)** Superficial velocity air. Normalized with $U_{inlet-air}$.
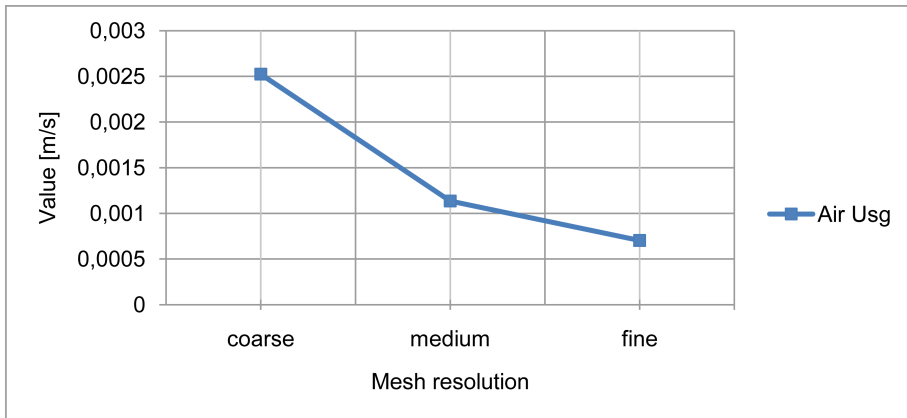
Figure 5.2: Grid dependency.

Figure 5.3: Variation of pressure at the inlet at different grid refinements.

No obvious trends are visible from the plots in figure 5.2. For both pressure and superficial velocity the difference is minimal. As the inlet is given a velocity and the outlet a pressure, the pressure on the inlet is mainly influenced by the grid. Figure 5.3 shows that the pressure at the inlet decreases as the refinement increases. A mesh is intended to be a representation of the real thing, and as the resolution increases, the closer to the real thing it gets. So the mesh is thought to gradually converge as the mesh resolution is increased. One can therefore conclude that the mesh resolution should be even higher than used here. In addition, a brief look at the residuals can give an good indication on how good the grid is performing. For this test, all the simulations reach a good convergence level after $\approx$ 250 iterations. Convergence level is set to 10^{-4}. The different meshes are run with maximum number of iterations set to 1000 iterations, with a minimum set to 200. Also the pressure difference between outlet and inlet is monitored, and the simulations where stopped after fulfilling these criteria of minimum number of iterations, convergence target and no pressure oscillations between outlet and inlet. Both the coarse and the fine grid suffers from numerical diffusion at the first few iterations. This do not necessarily mean that there is something wrong with the grids, since it is not present at later iterations, but give an indication on the grid quality. Numerical diffusion is less present for the simulation on the medium sized grid.
Certain areas in this model is more sensitive to the mesh refinement, and it is important to evaluate these areas carefully. Point 5 and 6 (figure 5.1) is in the near vicinity of the wall, and suits good for extra attention. Figure 5.4 shows the relative pressure and the superficial velocity of air in point 5.

(a) Relative pressure in point 5

(b) Superficial velocity air. Normalized with $U_{inlet-air}$.

Figure 5.4: Grid dependency at point 5.

Relative pressure at point 5 in figure 5.4a shows the same tendency to decrease with increasing refinement as in figure 5.3, and with the same conclusion. For the superficial velocity it tends to converge after the medium sized mesh.

The outset for this analysis was to see if choice of mesh will influence the solution in any large degree. From these results it is difficult to say which mesh is the best to use. The results shows small deviations between each other. With the emphasis on making a model as cheap computationally as possible, and still get reasonable good results, the medium sized mesh is chosen. The choice is thought to give a good compromise between near wall resolution, i.e. boundary layer resolution and available computer recourses. In Versteeg et. al. [1] and Roache [29] methods for quantifying numerical errors are presented. These methods are similar to the method used in the present authors project

thesis [6]. It is chosen not to use these methods here as they are thought to serve the similar purpose as the analysis presented above. Also, the mesh check function in Ansys Mesh leaves a smaller window for errors when creating the mesh compared to older software.

5.1.2   CFD results

Setup for the CFD simulations is given in appendix F. The case for an angle of attact at 10° and $U_{inlet} = 70m/s$ is presented here, since this case resembles the experiments. For the other cases, it is presented briefly in a similar manner in appendix G.

Figure 5.5 displays contour plots of superficial velocity of air and the shared pressure field taken at the mid-span of the channel at t= 0.4s.

(a) Superficial velocity air   **(b)** Pressure
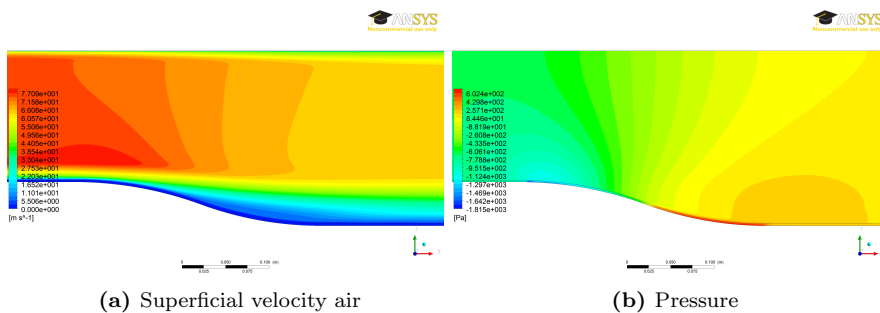
Figure 5.5: Countour plots of superficial velocity and pressure over the profile section at t= 0.4s.

Not surprisingly there is a increase in pressure and a decrease in velocity as the channel diverges. When comparing to the case with only air, it is clear to see that the liquid film imposes a big velocity difference in the near vicinity of the surface. Figure 5.6 illustrates this for a velocity profile taken at the midspan ($z = 0.02$) of the channel. The profile for the case with liquid film is taken from the interface at $\approx$ 2mm from the solid surface and 50mm up, whilst the other is taken from the solid surface and 50mm up.
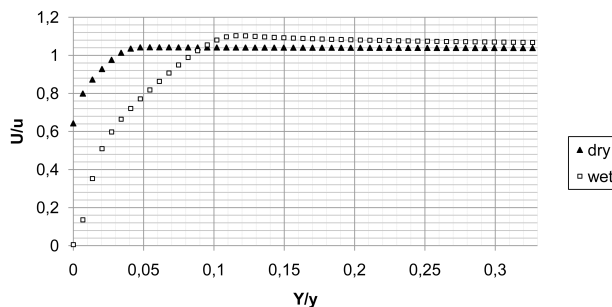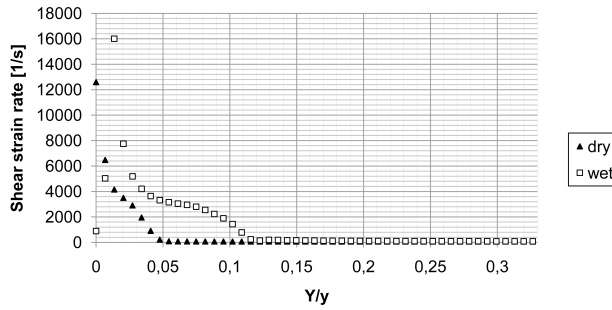

Figure 5.6: Velocity profiles for single and two-phase at $x = -0.15m$ in the inlet section. Values are normalized with the inlet velocity of air and the height of the channel.

Higher velocity in the the free stream for the wet case is thought to be due to a decrease in cross sectional area and a increase in frictional losses at the interface caused by the rough liquid film. For the case with the liquid film, there is a lower velocity at the surface and a weaker velocity gradient out to the free stream. By looking at the shear strain rate profiles in figure 5.7 of air at the same point, it is clear that the liquid film case gives a lower value close to the wall ($Y/y < \approx 0.01$). Shear strain rate relates to the shear stress by:

$$\varsigma = \frac{\tau_w}{\mu} \tag{5.1}$$

where ς is the shear strain rate, τ_w is the shear stress and μ is the viscosity of the fluid.

Figure 5.7: Shear strain rate profiles for single and two-phase at $x = -0.15$m in the inlet section.

In White[14] and other textbooks it is given that the point of separation is where τ_w is zero. This means that the gas phase over the liquid film is closer to the criterion for separation. Figure 5.8 shows the shear strain rate plotted when subjected to an adverse pressure gradient over the profile section at $x = 0.14$m.
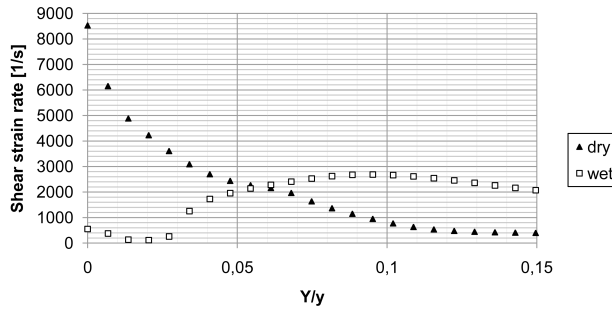
Figure 5.8: Shear strain rate profiles subjected to an adverse pressure gradient at $x = 0.14$m.

Here, it is even more clear that the shear strain rate for the wet case is lower, and therefore more susceptible to separation of the gas boundary layer. It is however from these simulations difficult to conclude if there is separation over the profile for the wet case.

Figure 5.9 shows the velocity profile at $x = 0.14$m close to the liquid film.
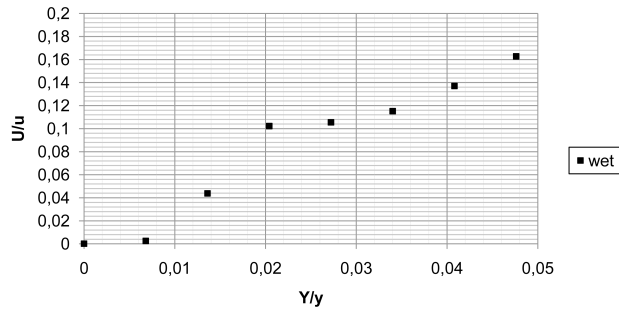
Figure 5.9: Velocity profile over the profile section.

As seen in figure 5.9 the velocity near the wall is close to zero, supporting the theory that the gas boundary layer is fragile in this region.

5.2　Experimental work

Maintenance on the wet gas compressor facility has set restrictions to the time spent on the experimental work in this thesis. It is was therefore chosen to confine the experimental work, and concentrate to get valuable results. The outset was to follow the test matrix in appendix H. The experiments where conducted with one volume flow, one angle of attack and one liquid flow rate. In addition, initial tests will serve as a important part of the results.

5.2.1　High speed camera

The Fastcam 1024PCI (see appendix I) was used during the laboratory experiments together with a Nikon D70s SLR still camera for documentation purposes. The high speed camera was set to capture 3000 fps during the tests. Fastcam 1024PCI was equipped with a Nikkor 50mm f1.2 lens, while the Nikon D70s was equipped with a Sigma 17-70mm f2.8-4.5 zoom lens. Pictures are edited in Adobe Photoshop CS5. Some initial visual observations are presented first.

Figure 5.10 shows the flow field in the channel at a gas volume flow of $\dot{Q}_g = 0.38 m^3/s$ and water mass flow of $\dot{m}_l = 0.11 kg/s$.
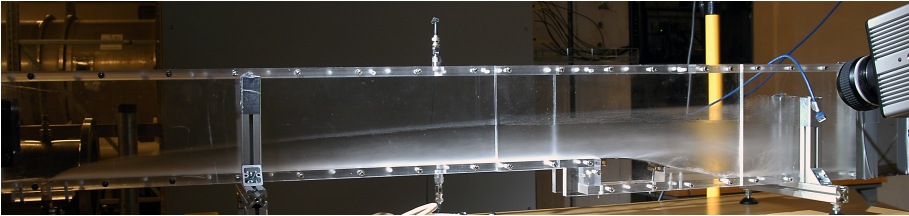
Figure 5.10: Overview of the flow field in the channel at test conditions.

From figure 5.10 it is clear to see that the flow field is somewhat semi-annular. Water is adhering to the walls, and forming a thin liquid film, leading to blocking of the optical access at the side walls. This was not visible in the initial tests, and is to be explained by a significant increase in gas velocity and an increase in water flow rate and pressure.

Figure 5.11 shows a closer look on the flow field at the area of interest.
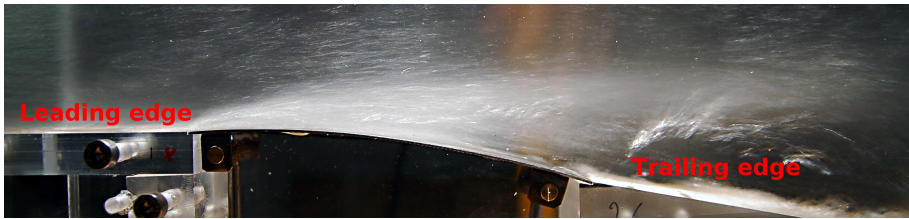
**Figure 5.11:** Flow field over the area of interest.

From figure 5.11 it seems like there is a high concentration of dispersed droplets initiated at the start of the profile section. Also, a significant liquid hold-up is spotted at the trailing edge of the profile. These observations, together with the evolution of a semi-annular regime are mainly related to manufacturing and design imperfection, and are discussed in chapter 7.

The Fastcam was focused perpendicular to the right wall of the channel as figure 5.12 illustrates.
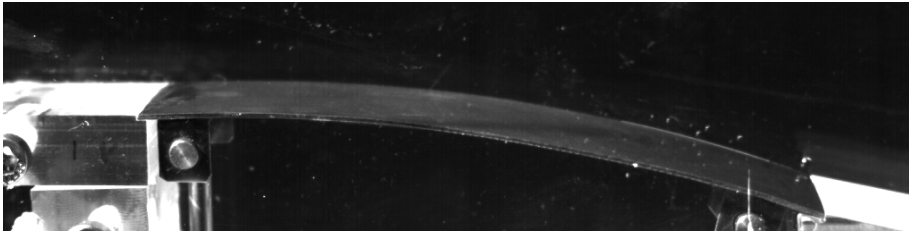
Figure 5.12: Field of view of the Fastcam.

As discussed earlier, the visual access on the area of interest was obscured by the liquid film on the walls. Disregarding the lack of vision directly onto the profile, figure 5.13 shows a interesting "void" towards the trailing edge.
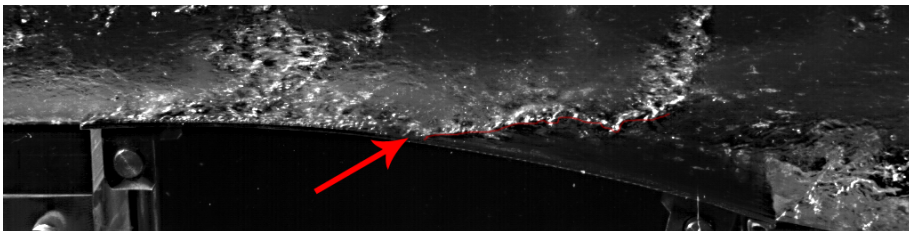
Figure 5.13: Picture showing a clear "void" indicated by the red arrow, moving towards the trailing edge of the profile.

In this void, observations shows there are an evident deceleration of the liquid film and droplets. Liquid was ejected vertically up and out into the free-stream, indicating that there is lower velocities in this region. These observation are shown in the picture sequence in figure 5.14 on the next page.

(a)   (b)

(c)   (d)

(e)   (f)
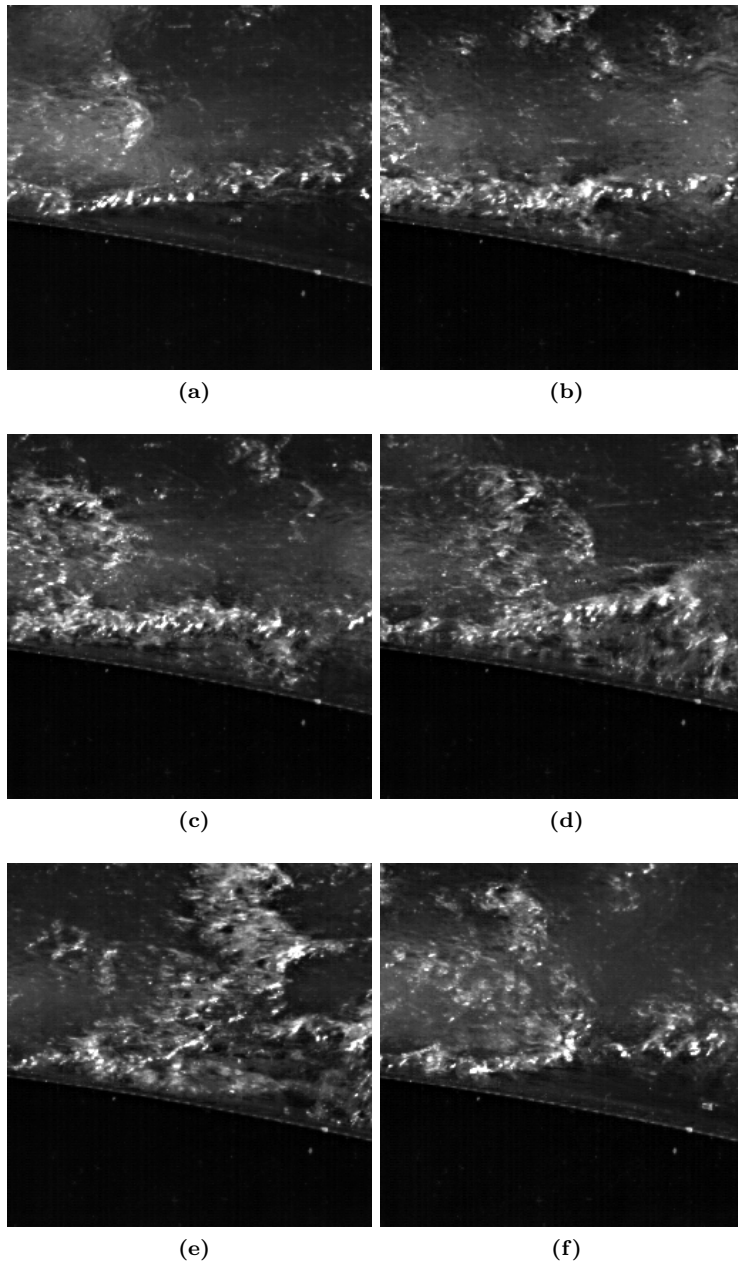
Figure 5.14: Ejection of liquid out from the void.

These observations are interesting due to the fact that a reduced velocity in these regions implies that the boundary layer inertia is decreased, and is more susceptible to separation. The diverging geometry of the channel also gives an adverse pressure gradient, which gives a negative contribution to the stability of the boundary layer.

In figure 5.15, a picture of the liquid film patter is given.

Figure 5.15: Liquid film pattern over the profile section. The red arrow indicating the trailing edge.

The liquid film structure over the profile section, showing a highly irregular pattern towards the trailing edge. Just before the trailing edge, the film structure gets smoother. As discussed earlier in chapter 2 the wave structure is highly dependent on the relative velocity between the two phases, it therefore supports the theory that there is a decrease in gas velocity in this region. It is noted that the point where the liquid surface gets smoothened do not cohere with the point where the void is spotted. This can be explained by instantaneous differences, since the pictures is not taken at the exact same time.

Another important discovery that emphasizes the previous observations are the prominent two-dimensional wave structure, or roll waves traveling at the side walls. These waves dissolve when traveling over the curved section. This is depicted in figure 5.16.
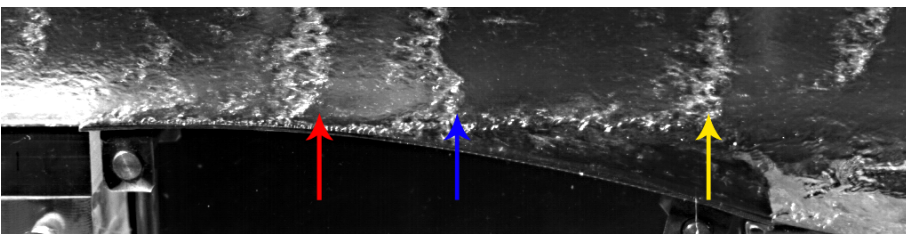
Figure 5.16: Break-up of two-dimensional waves.

The red arrow indicating a nearly perfect two-dimensional pattern, whilst the blue and yellow ones are showing the development and break-up of a typical wave, respectively. Mainly two mechanisms is thought to cause this break up, acting together or alone. Adverse pressure gradients acting on the waves can cause an already unstable film to change pattern. Last but not least, if there

is a separation bubble over the profile, this will cause the free flow to speed up
due to the decreased effective flow area. Hence, the change in relative velocity
between the two phases will cause a transition from the two-dimensional roll
waves to atomization of the wave as discussed in chapter 2.

Although these visual observations is promising and very interesting, it is
difficult to conclude without any credible measurements of the velocity at a
boundary layer level. But as the pictures show, high speed camera recording
has proven to be an excellent tool for visual observations, and a good starting
point for learning more about the complex nature of multi-phase flows.

5.2.2   FFT-analysis

Results from the FFT-analysis is from both initial tests described in appendix
D, and from the main test. Results from the initial test will be presented first.

In the initial test the FFT-analysis was conducted on a gas turbine filter rig,
with a substantial lower velocity. The gas (air) velocity was assumed to be
in the range of $\approx 15 - 20m/s$. Constant rotational speed was held. Due to
extensive leakages on the rig the assumed velocity will only serve as an in-
dicative parameter. Three different mass flows of water were run, indicated as
low, medium and high. Liquid flow was controlled by a faucet, so no accurate
readings were available. The FFT method were included in LabView with a
high-pass filter at 5Hz to exclude large amplitudes at low frequencies that are
caused by the offset of the raw signal.

Figure 5.17 shows waterfall graphs of the frequency spectra for the low wa-
ter flow.
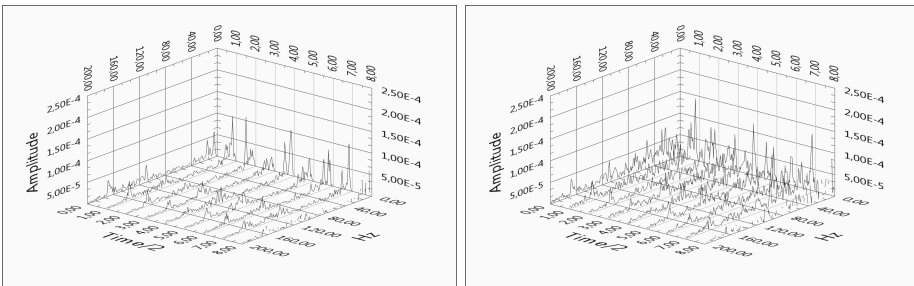
(a) Dry side.   (b) Wet side.

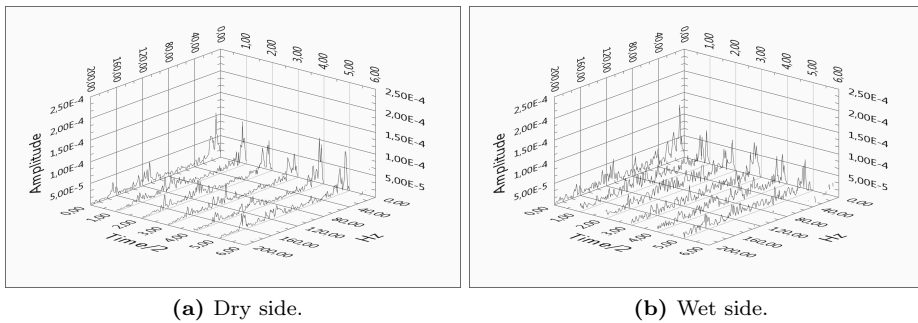**Figure 5.17:** Frequency spectra for low water flow.

Figure 5.17 shows large amplification on the lower frequencies on the wet
side, compared to the dry side. The disturbances is thought to be a result of
the liquid film. Water has a higher density than water, and it is evident that
it gives a larger contribution to the perturbations than air alone.

Figure 5.18 shows the frequency spectra for the case of medium water flow.

(a) Dry side.

(b) Wet side.
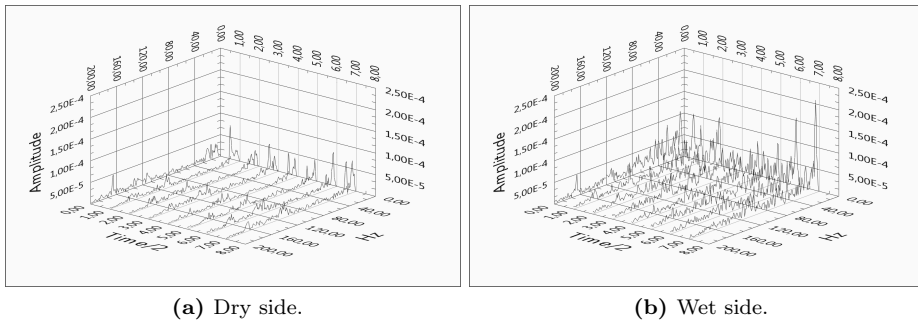
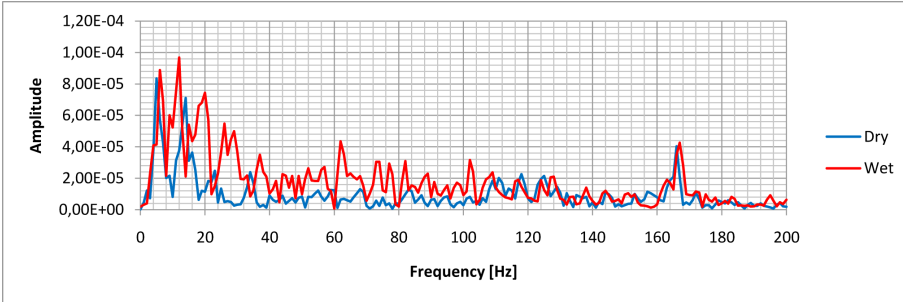**Figure 5.18:** Frequency spectra for medium water flow.

Same observations is present here, but it is difficult to distinguish any changes due to the increased water flow. In figure 5.19 the case for high water flow is shown.

(a) Dry side.

(b) Wet side.

Figure 5.19: Frequency spectra for high water flow.

Here, it is an evident decrease in amplitude on the wet side. The increased water flow seems to have a stabilizing effect on the frequency spectra on the wet side. However, it is difficult to conclude that these damped oscillations are solely due to the liquid film. One theory can be that the increased liquid hold up (film thickness) acts as a damper on the sensors. Another can be that the pressure in the channel decrease slightly due to increase in volumetric fraction of water. The pressure sensors used can operate in the range from 0 to 250 bar, and this may indicate that the sensor struggle to resolve small amplitudes that are present in figure 5.17, 5.18 and 5.19.

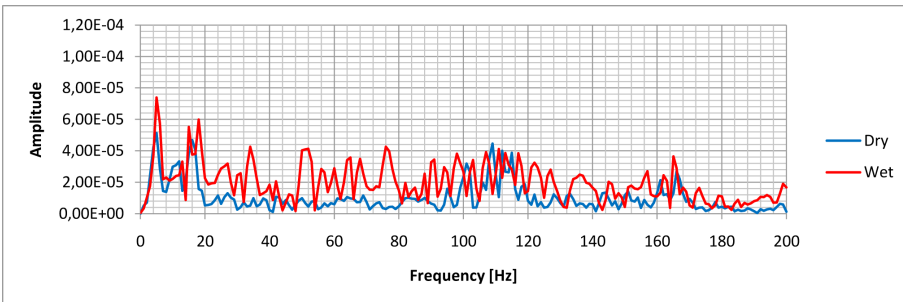In figure 5.20 the frequency spectra for the three different cases at an in-
stance ($t = 3s$) are plotted.

(a) Low liquid flow
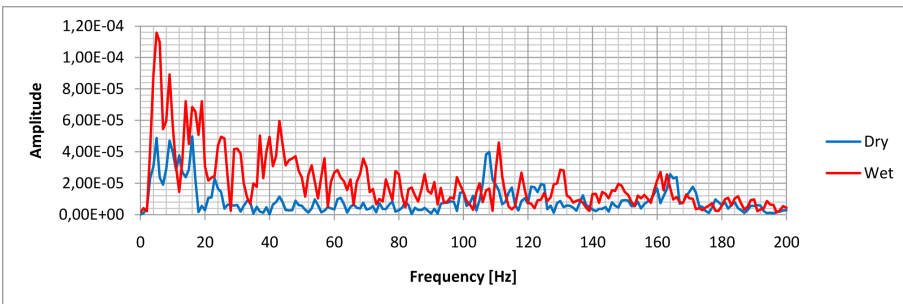
(b) Medium liquid flow

(c) High liquid flow

Figure 5.20: Frequency spectra for the three different cases.

Again, it is clear that the liquid film damps the oscillations in the low fre-
quency range of approximately 20-100Hz.

Figure 5.21 shows the frequency spectra for the main experiments con-
ducted on the wet gas test facility described in chapter 4. At this test, the
water mass flow was set to $\dot{m}_l = 0.11 kg/s$ and volumetric flow, $\dot{Q}_g = 0.38 m^3/s$.
Note that the amplitude axis range in figure 5.21 is the same as in the initial

(a) Dry side.   (b) Wet side.
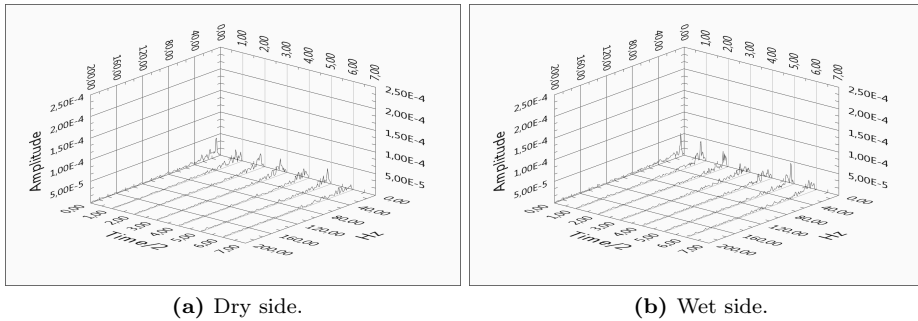
Figure 5.21: Frequency spectra for main test. Water flow was measured to
$\dot{m}_l = 0.11 kg/s$.

tests described above. Wet and dry side shows striking similarity. No tendency
to stabilizing effects is visible here. Again, the assumption is here that the de-
crease in pressure due to even higher velocities is causing even lower deflection
on the signal. Even when decreasing the axis range, no observations similar to
that in the initial tests can be seen.

6   Discussion

This chapter will serve as a summary of the results presented in chapter 5.

The CFD simulations and the high speed photography shows some similarities by visual observations. Both show a low velocity region towards the trailing edge of the profile. Observations from the high speed camera recordings shows a crisp void at the rear of the profile, together with a much smoother liquid film in this region. These observations render the possibility that there is separation over the profile section. Results from the CFD simulations also reveal a substantial lower shear strain rate for the air phase over the liquid film than for air alone over a solid surface. This implies that the liquid film imposes a greater susceptibility for the gas phase to separate when subjected to an adverse pressure gradient. No boundary layer separation was detected from the CFD simulations.

The FFT-analysis was a stand-alone experiment which gave interesting results. The frequency spectra shows a damping behavior on the wet side when increasing the mass flow of water in the initial experiments. This damping behavior is however not visible on the spectra from the main experiment on the wet gas compressor rig. This is thought to be due to a substantial decrease in pressure from the initial tests, leading to questions regarding the sensitivity of the dynamic pressure sensors below atmospheric pressure. This question has not been successfully answered, even though correspondence with the vendors [30] has been carried out.

7   Recommendations for further work

This chapter will present advices for further work on subjects that are discussed in this thesis.

CFD-model

Although the CFD-model used in this thesis shows very promising capabilities on multiphase flows, it is clear that an even finer grid would be preferred. Due to the lack of computational resources during this thesis, this has not been accomplished. The lack of spotting boundary layer separation over the liquid film is solely thought to be due to the near wall refinement of the mesh. A supercomputer like Kongull at NTNU is readily available for users of Ansys Fluent, and should be considered. Increased resources would also give the opportunity to implement even more sophisticated models, like the inhomogeneous multiphase alternative discussed in chapter 2 and various heat transfer models. With enhanced processing capabilities, the possibility of using even more advanced turbulence modeling, like LES (Large Eddy Simulation) should also be considered.

Experimental

The use of Plexiglas on the test model has proven to be a success. The material is relatively cheap, easy to adapt and gives great optical access to the flow. Plexiglas should be considered used in further experimental models. The experimental model used in this thesis has proven to be to narrow. Liquid deposition on the side walls of the channel has been prominent, leading to degradation of the optical access on the area of interest. The water injection module should also take much of the blame for this. High liquid flow rate and high gas velocity sprayed the liquid out from the injection module into the channel instead of at the channel floor, which was wanted initially. The need for controlling the ejection angle of the liquid is evident. A thin adjustable flat plate over the injection module, parallel to the channel floor should prevent the liquid from ejecting out into the channel. Moving the injection module further downstream should also be considered, and thus avoiding strong turbulence generated by the sharp corners of the channel inlet. The profile section should be manufactured as one piece, and therefore avoiding sharp edges at the connection between the channel floor and the bricks. The last suggestion for improvement on the test channel used in this thesis is to coat the inside of the channel with a transparent film to eliminate any sharp edges created by the assembled plates. Sharp edges is a recurring problem, as also mentioned and documented in chapter 5.

For the future study of boundary layer separation over a thin liquid film, scientific measurement techniques should be used. In order to carry out this, the channel must be re-designed. A channel with a quadratic cross section with good visual access from all sides is obvious. Experiments and measurements

at lower gas velocities without any entrainment should be tried carried out to be compared to the case with only air. This to increase the knowledge on the influence of film roughness to the gas boundary layer. Without any liquid entrainment, the hot wire anemometry measurements could be a good alternative.

Regarding dynamic pressure measurements, it is evident that a study on different sensors should be carried out first to clarify the applicability for experiments done in this thesis.

References

[1] H.K. Versteeg and W. Malalasekera. *An Introduction to Computational Fluid Dynamics, the Finite Volume Method.* Pearson Prentice Hall, 2007.

[2] ANSYS Inc. *ANSYS CFX 13.0 Documentation*, 2010.

[3] Joachim Mossige, EDR. E-mail and phone correspondence. Written and oral, 2011.

[4] Bernard Müller. Introduction to Computational Fluid Dynamics, 2008.

[5] ANSYS Inc. *ANSYS FLUENT 12.0 Documentation*, 2009.

[6] Tarjei Thorrud Larsen. Strømning i våtgasskompressor. Project thesis NTNU, 2010.

[7] D. Schubring and T.A. Shedd. Critical friction factor modeling of horizontal annular base film thickness. *International Journal of Multiphase Flow*, 35:389 – 397, 2009.

[8] T.S. Ng, C.J. Lawrence, and G.F. Hewitt. Friction factors in stratified two-phase flows. *Chemical Engineering Research and Design*, 82(3):309 – 320, 2004. Fluid Flow.

[9] Håvard Skomedal Torvanger. Wet gas compression fundamentals. Master's thesis, Norwegian University of Science and Technology, 2010.

[10] I. Kataoka, M. Ishii, and A. Nakayama. Entrainment and desposition rates of droplets in annular two-phase flow. *International Journal of Heat and Mass Transfer*, 43(9):1573 – 1589, 2000.

[11] G.F. Hewitt and N.S. Hall-Taylor. *Annular Two-Phase Flow.* Pergamon Press, 1970.

[12] Christopher E. Brennen. *Fundamentals of Multiphase Flows.* Cambridge University Press, 2005.

[13] M. Ishii and M. A. Grolmes. Inception criteria for droplet entrainment in two-phase concurrent film flow. *AIChE Journal*, 1975.

[14] Frank M. White. *Fluid Mechanics, 5th ed.* McGraw-Hill, 2003.

[15] E. T. Hurlburt and T. J. Hanratty. Prediction of the transition from stratified to slug and plug flow for long pipes. *International Journal of Multiphase Flow*, 28(5):707 – 729, 2002.

[16] R.J. Belt, J.M.C. Van't Westende, and L.M. Portela. Prediction of the interfacial shear-stress in vertical annular flow. *International Journal of Multiphase Flow*, 35(7):689 – 697, 2009.

[17] John J. Bertin and Russel M. Cummings. *Aerodynamics For Engineers, 5th ed.* Pearson Prentice-Hall, 2009.

[18] R. A. Antonia and P-Å. Krogstad. Turbulence structure in boundary layers over different types of surface roughness. *Fluid Dynamics Research*, 28(2):139 – 157, 2001.

[19] Carolyn D. Aubertine, John K. Eaton, and Simon Song. Parameters controlling roughness effects in a separating boundary layer. *International Journal of Heat and Fluid Flow*, 25(3):444 – 450, 2004. Turbulence and Shear Flow Phenomena (TSFP-3).

[20] Frank M. White. *Viscous Fluid Flow.* McGraw-Hill, 2006.

[21] Trond G. Grüner and Lars E. Bakken. Aerodynamic instability investigation of a centrifugal compressor exposed to wet gas. *ASME*, 2010.

[22] Lars Brenne. *Straight-Walled Diffuser Performance.* PhD thesis, NTNU, 2004.

[23] Trond G. Grüner, Lars E. Bakken, Lars Brenne, and Tor Bjørge. An experimental investigation of airfoil performance in wet gas flow. *Proceedings of ASME Turbo Expo 2008: Power for Land, Sea and Air*, 2008.

[24] Anthony J. Wheeler and Ahmad R. Ganji. *Introduction to Engineering Experimentation.* Pearson Education, 2004.

[25] Stein Tore Johansen, SINTEF. Conversation. Oral, 2010.

[26] F.R. Menter. Two-equation eddy-viscosity turbulence models for engineering applications. *AIAA Journal*, 1994.

[27] Mads Herbert, VIDIX. E-mail and oral correspondence. Written and oral, 2010-2011.

[28] M. Honkanen and Pentti Saareninne. Mulphase piv method with digital object separation methods. *5th International Symposium on Particle Image Velocimetry*, 2003.

[29] Patrick J. Roache. *Verification and Validation in Computational Science and Engineering.* Hermosa Publishers, 1998.

[30] Jostein Kyte, Scanditest. E-mail correspondence. Written, 2011.

A   Derivation of governing equations

The Nabla operator given in equation 2.2, 2.3 and 2.5 is given by:

$$\nabla = \left[\frac{\partial}{\partial x}, \frac{\partial}{\partial y}, \frac{\partial}{\partial z} \right] \tag{A.1}$$

This yields for a Cartesian coordinate system.

Gradient

For any scalar function $\varphi(x, y, z)$, the gradient for φ is defined as:

$$\nabla \varphi = \frac{\partial \varphi}{\partial x} \mathbf{i} + \frac{\partial \varphi}{\partial y} \mathbf{j} + \frac{\partial \varphi}{\partial z} \mathbf{k} \tag{A.2}$$

Divergence

The velocity is given as a vector:

$$\mathbf{U} = \begin{bmatrix} \mathbf{U}_x \\ \mathbf{U}_y \\ \mathbf{U}_z \end{bmatrix} \tag{A.3}$$

The superscript T is the transposed matrix, and for equation A.3 is given as:

$$\mathbf{U}^T = [\mathbf{U}_x \ \mathbf{U}_y \ \mathbf{U}_z] \tag{A.4}$$

The divergence of $\mathbf{U}$ is then:

$$\nabla \cdot \mathbf{U} = \frac{\partial \mathbf{U}_x}{\partial x} + \frac{\partial \mathbf{U}_y}{\partial y} + \frac{\partial \mathbf{U}_z}{\partial z} \tag{A.5}$$

Multiphase

For the density given in the transport equation 2.6 this yields:

$$\rho = \sum_{\alpha=1}^{N_p} r_\alpha \rho_\alpha \tag{A.6}$$

Where α denotes the phase of interest, N_p is the number of phases in the system and r_α is the volume fraction of phase α. The velocity U is given as:

$$U = \frac{1}{\rho} \sum_{\alpha=1}^{N_p} r_\alpha \rho_\alpha U_\alpha \tag{A.7}$$

and the diffusivity Γ is given as:

$$\Gamma = \frac{1}{\rho} \sum_{\alpha=1}^{N_p} r_\alpha \Gamma_\alpha \tag{A.8}$$
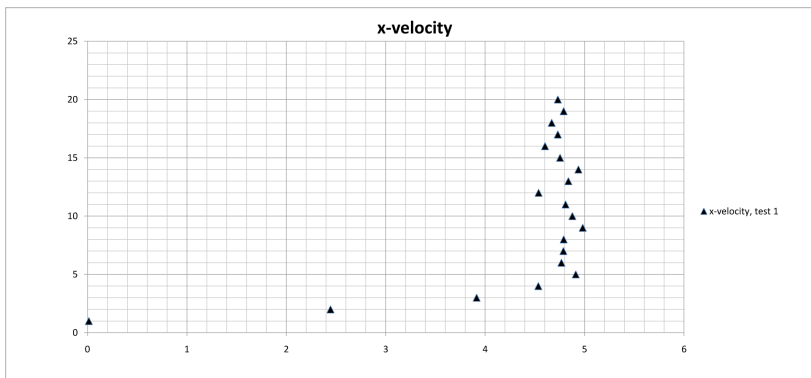
B Initial test - LDV

Figure B.1 shows the relative simple setup of the LDV system. The bottleneck in a LDV system is optical access to measurement area. Plexiglas turned out to be of sufficient quality. Figure B.2 shows the result from the test. The y-axis in the figure is not to be considered since the laser was traversed manually and not by a mechanical traversing device, which would give the accurate height increment for each point.
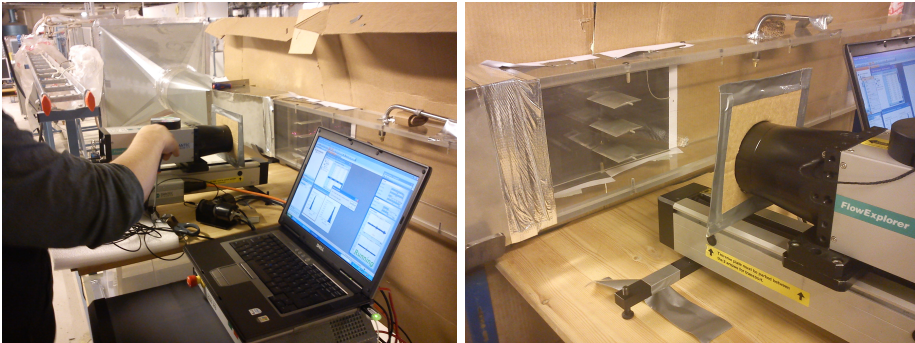
(a) The relative easy setup of a LDV-system, consisting of a laser and a computer.

(b) The area of interest is here the airfoil in the middle. From the upper surface and up.

Figure B.1: The measurements were done by traversing the laser vertically by hand. A mechanical traversing system is a lot more accurate and a must.


Figure B.2: Velocity profile over an airfoil from LDV measurements.

C Initial test - channel 1

The 23rd of March a initial test was conducted on the channel. The purpose for this test was to look for any water and air leakages, or other problems that could cause problems later.

This test was done on a gas turbine filter-rig, and therefore the air speed was significantly lower than on the wet gas compressor. Still, the test was able to spot leakages and sharp corners in the channel that was difficult to observe with the naked eye. The first problem was at a connection between two plates on the left wall. There was a clearly visible gap and air was sucked in. In addition, the gap produced a sharp corner on the inside of the channel. This resulted in a quite large liquid hold-up at the connection that led to droplet entrainment. At the connection between the curved profile and the channel floor there is also a noticeable liquid hold-up, that is most likely produced due to a small gap in the connection. These observations are shown in figure C.1.
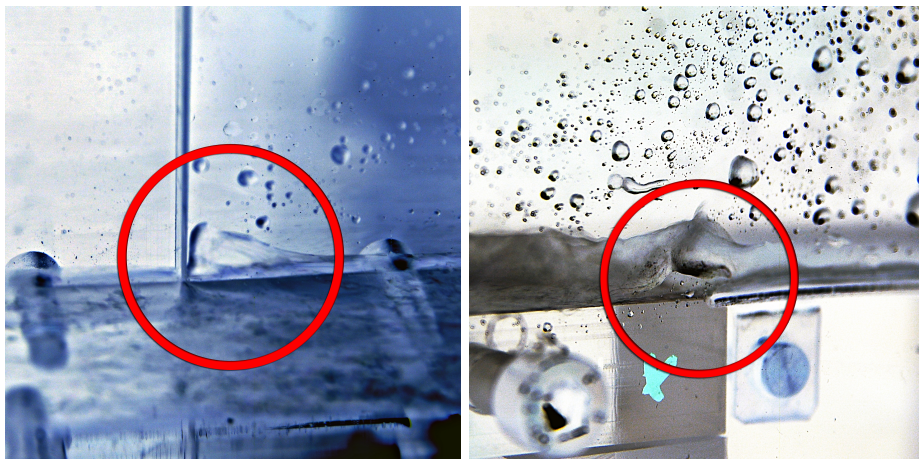

(a) Poor connection between two plates.   **(b)** Small edge on the connection between floor and the curved profile.

Figure C.1: The liquid hold-up at the connection between two wall plates and the connection between the curved profile and the channel floor is indicated by a red ring. One can also clearly see droplets deposit on the channel walls. The picture is in inverted color mode to see the water interface more clearly.

D   Initial test - channel test 2

The 30th of March the improvements done on the channel after the first test was checked. In addition to the improvements discussed in appendix C two Kistler dynamic pressure sensors (appendix E for data sheet) were mounted at the inlet section of the channel. They were mounted flush with the roof and floor of the channel as figure D.1 shows. Both sensors were mounted 700 mm from the inlet at the center of the channel.

This time, no leakages where found nor liquid hold-ups of any significance
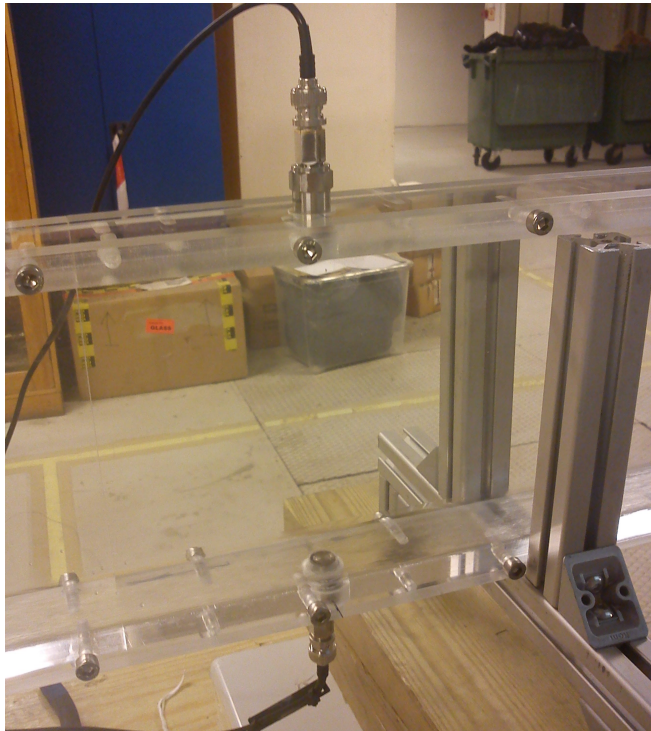
Figure D.1: Two Kistler dynamic pressure sensors mounted at roof and floor of the channel.

compared to the first test. The main purpose for mounting the pressure sensors is to look at the influence the wavy liquid film may have on the dynamic pressure in the channel. This relates to the earlier work of [21, Trond G. Gruner et al.] on predicting instabilities in a centrifugal compressor exposed to wet gas. In a wet gas compressor theres a highly annular flow, and by placing the pressure sensors on one "dry" and one "wet" side of the channel the hope is to see the difference in pressure oscillations and recognize instabilities due to the liquid film. The initial tests indicates larger amplitudes at low frequencies on the liquid film side as shown in figure D.2. The test was logged with a sampling rate of 20 kHz. A brief look at the two spectra it is easy to see that the

(a) Dry side **(b)** Wet side
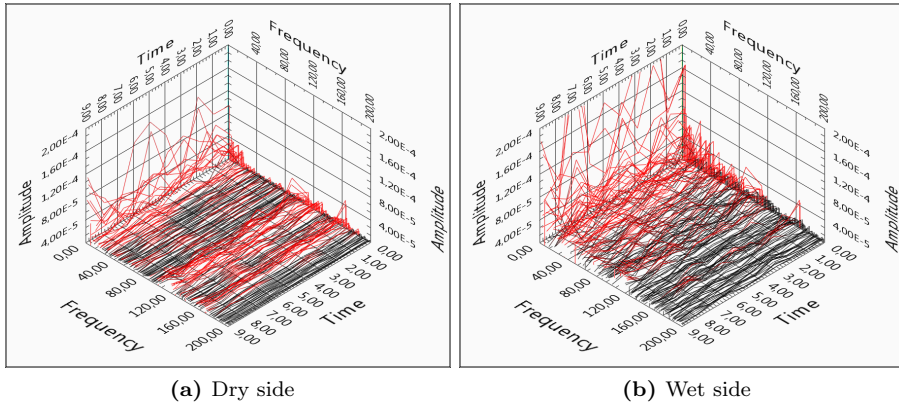
Figure D.2: The frequency spectrums of the two sides shows a significantly higher amplitudes on the wet side.

water film has some influence. Though it is not clear what causing the elevated fluctuations at this point without any visual observations. To determine the cause of these fluctuations synchronized visual observations with a high speed camera may be the key to understand this.

E   Data sheets for Kistler dynamic pressure sensor

At the next page the data sheets for the pressure sensors is attached.

Pressure – PAG

KISTLER

Quarz-Drucksensor, beschleunigungskompensiert
Capteur pression à quartz, avec compensation d'accélération
**Quartz Pressure Sensor, Acceleration-Compensated**

7031

Quarz Drucksensor zum Messen dynamischer und quasistatischer Drücke bis 250 bar bei Temperaturen bis 200 °C. Der eingebaute Beschleunigungssensor kompensiert Störsignale die durch Schock oder Vibration in Richtung der Sensorachse entstehen.

Capteur de pression à quartz pour mesurer des pressions dynamiques et quasistatiques jusqu'à 250 bar à des températures jusqu'à 200 °C. L'accéléromètre incorporé compense les signaux d'interférence provenant des chocs et vibrations dans la direction de l'axe du capteur.

Quartz pressure sensor for measuring dynamic and quasistatic pressures up to 250 bar at temperatures up to 200 °C. The built-in accelerometer compensates interference signals produced by shock or vibration in the direction of the sensor axis.

- Beschleunigungskompensiert
  Compensé aux accélération
  Accceleration compensated

- Hohe Empfindlichkeit
  Haute sensibilité
  High sensitivity

- Temperaturen bis zu 200 °C
  Températures jusqu'à 200 °C
  Temperatures up to 200 °C
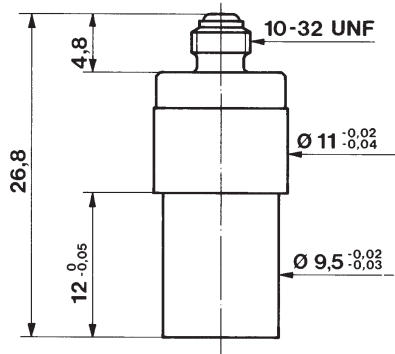
2:1

Technische Daten	Données techniques	Technical Data		
Bereich	Gamme	Range	bar	0 ... 250
Kalibrierte Teilbereiche	Gamme partielles étalonnées	Calibrated partial ranges	bar	0 ... 25
			bar	0 ... 2,5
Überlast	Surcharge	Overload	bar	350
Empfindlichkeit	Sensibilité	Sensitivity	pC/bar	≈ –55
Eigenfrequenz	Fréquence propre	Natural frequency	kHz	≈80
Linearität	Linéarité	Linearity	%FSO	≤ ±1
Beschleunigungsempfindlichkeit	Sensibilité aux accélérations	Acceleration sensitivity	bar/g	<0,0001
Betriebstemperaturbereich	Gamme de température d'utilisation	Operating temperature range	°C	-150 ...200
Temperaturkoeffizient der Empfindlichkeit	Coefficient de température de la sensibilité	Temperature coefficient of sensitivity	%/°C	0,02
Isolationswiderstand	Résistance d'isolement	Insulation resistance	TΩ	≥10
Stossfestigkeit	Résistance au choc	Shock resistance	g	5000
Kapazität	Capacité	Capacitance	pF	20
Gewicht	Poids	Weight	g	10,8
Stecker, Teflon-Isolator	Connecteur, isolateur en téflon	Connector, teflon insulator		10-32 UNF

1 N (Newton) = 1 kg·m·s^{-2} = 0,1019... kp = 0,2248... lbf; 1 kp = 1 kgf = 9,80665 N; 1 inch = 25,4 mm; 1 kg = 2,2046... lb; 1 Nm = 0,73756... lbft

* In all Kistler documents, the decimal sign is a comma on the line (ISO 31-0:1992).

Beschreibung

Der zu messende Druck wirkt über die Membrane auf das Quarzkristall-Messelement, das den Druck p (bar) in eine elektrische Ladung Q (pC = pico-Coulomb) umwandelt. Die Membrane aus rostfreiem Stahl ist mit dem Sensorgehäuse aus rostfreiem Stahl hermetisch und bündig verschweisst. Das durch die Masse des Sensors bei Beschleunigung (Schock oder Vibration) erzeugte Signal wird durch das Signal mit umgekehrten Vorzeichen eines eingebauten Beschleunigungssensors kompensiert.

Der Stecker-Anschluss ist mit dem Gehäuse verschweisst, jedoch ist sein Teflon-Isolator nicht völlig dicht.

Description

Par l'intermédiaire du diaphragme, la pression agit sur l'élément de mesure à quartz qui transforme la pression p (bar) en charge électrique Q (pC = pico-Coulomb). Le diaphragme en acier inoxydable est soudé hermétiquement, au ras du front, au boîtier en acier inoxydable. Les signaux dûs aux accélérations (choque ou vibrations) sont compensés par un signal de polarité inverse provenant d'un accéléromètre compensateur incorporé.

La prise électrique est soudée au boîtier, cependant son isolateur en téflon n'est pas rigoureusement étanche.

Description

The measured pressure acts through the diaphragm on the quartz crystal measuring element, which transforms the pressure p (bar) into an electric charge Q (pC = pico-Coulomb). The stainless steel diaphragm is welded flush and hermetically to the stainless steel sensor housing. The signal produced by acceleration (shock or vibration) due to the sensor mass, is compensated by a signal of inverse polarity yielded by the built-in accelerometer.

The connector is welded to the body, but its teflon insulator is not absolutely tight.

Kistler Instrumente AG Winterthur, CH-8408 Winterthur, Switzerland, Tel. (052) 224 11 11   Kistler Instrument Corp., Amherst, NY 14228-2171, USA, Phone (716) 691-5100

Anwendung

Der Drucksensor Typ 7031 eignet sich besonders für die Messung schneller Druckverläufe an stark vibrierenden Messobjekten. Dieser Sensor ist rund 10 mal weniger vibrationsempfindlich als der Standardsensor Typ 601A. Bei besonders beschränkten Einbauverhältnissen oder sehr hohen Messfrequenzen ist der Drucksensor 6031 zu verwenden.

Application

Le capteur type 7031 est adapté à la mesure de variations rapides de pression dans des dispositifs vibrant. Ce capteur est à peu près 10-fois moins sensible aux vibrations que le capteur standard type 601A. On choisit le capteur miniature 6031 pour des dispositifs à dimensions réduites ou pour les fréquences très élevées.

Application

The quartz pressure sensor Type 7031 is suited for dynamic pressure measurements on heaving vibrating objects. This sensor is about 10 times less sensitive to vibrations than the standard Type 601A. For very high frequencies or reduced mounting space the sensor 6031 is used.

Montage

Der Sensor kann mittels eines Montagenippels (Fig. 1) oder eines Steckernippels (Fig. 2) im Messobjekt oder dem Adapter montiert werden. Bei der Montage nach Fig. 2 werden Sensor und Steckernippel zu einer Montageeinheit zusammengeschraubt. Die Trennfläche kann mit "Loctite" gedichtet werden.

Siehe auch Datenblätter für:

Werkzeuge	4.012
Adapter	4.016
Steckernippel	4.014
Kabel	15.035

Montage

Le capteur peut être monté directement dans le dispositif de mesure ou dans l'adaptateur à l'aide d'un écrou de montage (fig. 1) ou d'un écrou connecteur (fig. 2). Pour le montage selon fig. 2, le capteur et l'écrou connecteur forment une unité. La jonction capteur - écrou connecteur peut être rendue étanche avec du "Loctite".

Voir aussi les notices techniques suivantes:

Outillage	4.012
Adaptateurs	4.016
Ecrous connecteurs	4.014
Câbles	15.035

Mounting

The sensor can be mounted directly into the measuring object or the adapter by means of a mounting nut (fig. 1) or a connecting nipple (fig. 2). When mounted with a connecting nipple, the latter is preassembled with the sensor to a mounting unit. The junction between nipple and sensor can with sealed by "Loctite".

See also datasheets for:

Tools	4.012
Adapters	4.016
Connecting nipples	4.014
Cables	15.035
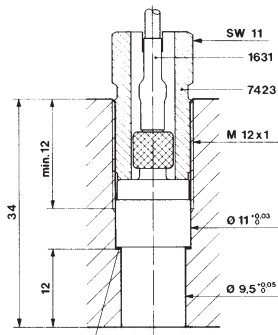
Fig. 1: 1135 / 1137
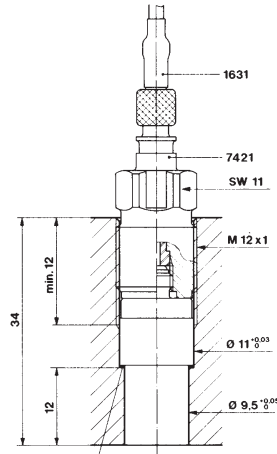
Fig. 2: 1135 / 1137

Zubehör	Typ
Cu-Dichtung	1135
Ni-Dichtung	1135A
Teflon-Dichtung	1137
Schlüssel für Steckernippel 7421	1303
Stufenbohrer	1333
Ausziehwerkzeug für 10-32 UNF	1311
Montagenippel SW8	7423
Steckernippel 10-32UNF/10-32UNF	7421
Steckernippel 10-32UNF/BNC	7401
Steckernippel 10-32UNF/TNC	7411
Steckernippel luftgekühlt 10-32UNF/10-32UNF	7461
Schrumpfschlauch für Stecker	1021
Montageadapter M14 x 1,25	7501
Montageadapter M5	7503
Kühladapter M18 x 1,5	7505
Kühladapter M14 x 1,25	7507

Accessoires	Type
Joint en cuivre	1135
Joint en nickel	1135A
Joint en téflon	1137
Clé pour écrou connecteur 7421	1303
Aléseuse progressive	1333
Outil extracteur pour 10-32 UNF	1311
Ecrou de montage OCW8	7423
Ecrou connecteur 10-32UNF/10-32UNF	7421
Ecrou connecteur 10-32UNF/BNC	7401
Ecrou connecteur 10-32UNF/TNC	7411
Ecrou connecteur refroidi par air 10-32UNF/10-32UNF	7461
Gaine thermorétractable pour connecteur	1021
Adaptateur de montage M14 x 1,25	7501
Adaptateur de montage M5	7503
Adaptateur refroidi M18 x 1,5	7505
Adaptateur refroidi M14 x 1,25	7507

Accessories	Type
Copper seal	1135
Nickel seal	1135A
Teflon seal	1137
Key for connecting nipple 7421	1303
Step drill	1333
Extraction tool 10-32 UNF	1311
Mounting nut WS8	7423
Connecting nipple 10-32UNF/10-32UNF	7421
Connecting nipple 10-32UNF/BNC	7401
Connecting nipple 10-32UNF/TNC	7411
Connecting nipple air cooled 10-32UNF/10-32UNF	7461
Heat-shrink tubing for connector	1021
Mounting adapter M14 x 1,25	7501
Mounting adapter M5	7503
Cooling adapter M18 x 1,5	7505
Cooling adapter M14 x 1,25	7507

000-051m-07.96 (DB03.7031m)

Pressure – PAE

Polystable® Quarz-Hochtemperatur-Drucksensor
Capteur de haute pression à quartz Polystable® pour températures élevées
**Polystable® Quartz High Temperature Pressure Sensor**   **7001**

Quarz Drucksensor, zum Messen dynamischer und quasistatischer Drücke bis 250 bar bei Temperaturen bis 350 °C.

Capteur de pression à quartz pour mesurer des pressions dynamiques et quasistatiques jusqu'à 250 bar à des températures jusqu'à 350 °C.

Quartz pressure sensor for measuring dynamic and quasistatic pressures up to 250 bar at temperatures up to 350 °C.

- hohe Empfindlichkeit
  haute sensibilité
  hight sensitivity

- Temperaturen bis zu 350 °C
  Températures jusqu'à 350 °C
  Temperatures up to 350 °C
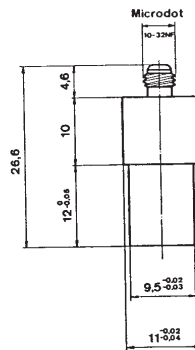
Technische Daten   Données techniques   Technical Data *

Bereich	Gamme	Range	bar	0 ... 250
Kalibrierte Teilbereiche	Gammes partielles étalonnées	Calibrated partial ranges	bar	0 ... 25
			bar	0 ... 2,5
Überlast	Surcharge	Overload	bar	350
Empfindlichkeit	Sensibilité	Sensitivity	pC/bar	≈ 80
Eigenfrequenz	Fréquence propre	Natural frequency	kHz	≈ 70
Linearität	Linéarité	Linearity	%FSO	<±0,8
Beschleunigungsempfindlichkeit	Sensibilité aux accélérations	Acceleration sensitivity		
axial	axiale	axial	bar/g	<0,002
radial	radiale	radial	bar/g	<0,0001
Betriebstemperaturbereich	Gamme de température d'utilisation	Operating temperature range	°C	–196 ... 350
Thermische Empfindlichkeitsänderung	Décalage thermique de la sensibilité	Thermal sensitivity shift		
20 ... 100 °C	20 ... 100 °C	20 ... 100 °C	%	≈+0,5
20 ... 350 °C	20 ... 350 °C	20 ... 350 °C	%	≈+3
200 ... ±50 °C	200 ... ±50 °C	200 ... ±50 °C	%	≈±1
Thermoschock	Choc thermique	Thermo shock		
bei 1500 min^{-1}, 9 bar p_{mi}	à 1500 min^{-1}, 9 bar pmi	at 1500 min^{-1}, 9 bar IMEP		
Δp	Δp	Δp	bar	< -0,7
Δp$_{mi}$	Δp$_{mi}$	ΔIMEP	%	< -5
Isolationswiderstand bei 20 °C	Résistance d'isolement à 20 °C	Insulation resistance at 20 °C	Ω	≥10^{13}
Stossfestigkeit	Résistance au choc	Shock resistance	g	5000
Gewicht	Poids	Weight	g	9
Stecker, Keramik-Isolator	Connecteur, isolateur céramique	Connector, ceramic insulator		10 - 32 UNF

1 N (Newton) = 1 kg·m·s^{-2} = 0,1019... kp = 0,2248... lbf; 1 kp = 1 kgf = 9,80665 N; 1 inch = 25,4 mm; 1 kg = 2,2046... lb; 1 Nm = 0,73756... lbft

*In all Kistler documents, the decimal sign is a comma on the line (ISO 31-0:1992).

Beschreibung

Der zu messende Druck wirkt über die Membrane auf das Quarzkristall-Messelement, das den Druck p (bar) in eine elektrische Ladung Q (pC = pico-Coulomb) umwandelt. Die Membrane aus rostfreiem Stahl ist mit dem Sensorgehäuse aus rostfreiem Stahl hermetisch und bündig verschweisst. Die Quarze sind in hochempfindlicher Anordnung (Transversaleffekt) in der Quarzkammer eingebaut, die mit dem Gehäuse hermetisch verschweisst ist.
Der Stecker ist dicht und hat einen Keramikisolator. Der Polystable® Quarz erlaubt eine Einsatztemperatur bis 350 °C.

Description

Par l'intermédiaire du diaphragme, la pression agit sur l'élément de mesure à quartz qui transforme la pression p (bar) en charge électrique Q (pC = pico-Coulomb). Le diaphragme en acier inoxydable est soudé hermétiquement, au ras du front, au boîtier en acier inoxydable. Les éléments à quartz sont montés en un ensemble de haute sensibilité (effet transversal) dans la chambre à quartz, elle-même soudé hermétiquement au boîtier.
La prise est étanche et possède un isolateur en céramique.
Le quartz Polystable® garantit une température d'utilisation jusqu'à 350 °C.

Description

The measured pressure acts through the diaphragm on the quartz crystal measuring element, which transforms the pressure p (bar) into an electrostatic charge Q (pC = pico-Coulomb). The stainless steel diaphragm is welded flush and hermetically to the stainless steel sensor body. The quartz elements are mounted in a highly sensitive arrangement (transversal effect) in the quartz chamber, which is welded hermetically to the body.
The connector is tight and has a ceramic insulator.
The Polystable® quartz allows an operating temperature of up to 350 °C.

Kistler Instrumente AG Winterthur, CH-8408 Winterthur, Switzerland, Tel. (052) 224 11 11   Kistler Instrument Corp., Amherst, NY 14228-2171, USA, Phone (716) 691-5100

Anwendung

Der Drucksensor Typ 7001 eignet sich besonders für die Messung schneller Druckverläufe. Er ist dem Typ 701A dort vorzuziehen, wo an der Einbaustelle Temperaturen bis 350 °C auftreten.

Typische Anwendungen:
Druckmessungen an Verbrennungsmotoren, Kompressoren, pneumatischen und hydraulischen Anlagen (ausgenommen Einspritzpumpen).

Montage

Der Sensor kann mittels eines Montagenippels (Fig. 1), oder eines Steckernippels (Fig. 2) im Messobjekt oder den Adapter montiert werden. Bei der Montage nach Fig. 2 werden Sensor und Steckernippel zu einer Montageeinheit zusammengeschraubt. Die Trennfläche kann mit "Loctite" gedichtet werden.

Siehe auch Datenblätter für:

Werkzeuge	4.012
Adapter	4.015
Steckernippel	4.014
Standardkabel	15.035
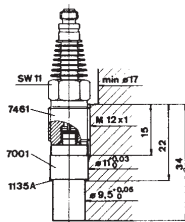
Application

Le capteur type 7001 est spécialement adapté à la mesure de variations rapides de pression dans des dispositifs de dimensions réduites. Il doit être utilisé - au lieu du type 701A - lorsque la température à l'emplacement de montage monte jusqu'à 350 °C.

Exemples d'applications:
Mesure de pressions de moteurs à combustion, compresseurs, installations pneumatiques et hydrauliques (à l'exception des pompes à injection).

Montage

Le capteur peut être monté directement dans le dispositif de mesure ou dans l'adaptateur à l'aide d'un écrou de montage (fig. 1) ou d'un écrou connecteur (fig. 2). Pour le montage selon fig. 2, le capteur et l'écrou connecteur forment une unité. La jonction capteur - écrou connecteur peut être rendue étanche avec du "Loctite".

Voir aussi les notices techniques suivantes:

Outillage	4.012
Adaptateurs	4.015
Ecrous connecteurs	4.014
Câbles	15.035

Application

The quartz pressure sensor Type 7001 is especially suited for dynamic pressure measurements on objects offering little mounting space. It must be used - instead of Type 701A - where the temperature of the mounting location reaches up to 350 °C.

Typical applications:
Pressure measurements on combustion engines, compressors, pneumatic and hydraulic installations (except injection pumps).

Mounting

The sensor can be mounted directly into the measuring object or the adapter by means of a mounting nut (fig. 1) or a connecting nipple (fig. 2). When mounted with a connecting nipple, the latter is preassemebled with the sensor to a mounting unit. The junction between nipple and sensor can be sealed with "Loctite".

See also datasheets for:

Tools	4.012
Adapters	4.015
Connecting nipples	4.014
Cables	15.035

Fig. 1:
Standard-Einbau
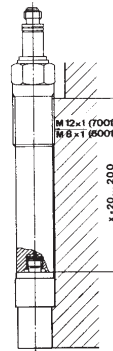Montage standard
Standard mounting

Fig. 2:
Spezialeinbau auf Anfrage
Montage spécial sur demande
Special mounting on request

Zubehör	Typ	Accessoires	Type	Accessories	Type
Cu-Dichtung	1135	Joint en cuivre	1135	Copper seal	1135
Ni-Dichtung	1135A	Joint en nickel	1135A	Nickel seal	1135A
Teflon-Dichtung	1137	Joint en téflon	1137	Teflon seal	1137
Schlüssel für Steckernippel 7421	1303	Clé pour écrou connecteur 7421	1303	Key for connecting nipple 7421	1303
Stufenbohrer	1333	Aléseuse progressive	1333	Step drill	1333
Ausziehwerkzeug für 10-32 UNF	1311	Outil extracteur pour 10-32 UNF	1311	Extraction tool 10-32 UNF	1311
Montagenippel SW8	7423	Ecrou de montage OCW8	7423	Mounting nut WS8	7423
Steckernippel 10-32UNF/10-32UNF	7421	Ecrou connecteur 10-32UNF/10-32UNF	7421	Connecting nipple 10-32UNF/10-32UNF	7421
Steckernippel 10-32UNF/BNC	7401	Ecrou connecteur 10-32UNF/BNC	7401	Connecting nipple 10-32UNF/BNC	7401
Steckernippel 10-32UNF/TNC	7411	Ecrou connecteur 10-32UNF/TNC	7411	Connecting nipple 10-32UNF/TNC	7411
Steckernippel luftgekühlt 10-32UNF/10-32UNF	7461	Ecrou connecteur refroidi par air 10-32UNF/10-32UNF	7461	Connecting nipple air cooled 10-32UNF/10-32UNF	7461
Schrumpfschlauch für Stecker	1021	Gaine thermorétractable pour connecteur	1021	Heat-shrink tubing for connector	1021
Montageadapter M14 x 1,25	7501	Adaptateur de montage M14 x 1,25	7501	Mounting adapter M14 x 1,25	7501
Montageadapter M5	7507	Adaptateur de montage M5	7507	Mounting adapter M5	7507
Kühladapter M18 x 1,5	7505	Adaptateur refroidi M18 x 1,5	7505	Cooling adapter M18 x 1,5	7505
Kühladapter M14 x 1,25	7507	Adaptateur refroidi M14 x 1,25	7507	Cooling adapter M14 x 1,25	7507

000-047m-09.95 (DB03.7001m)

F CFX setup

Detailed setup of the problem is shown in this appendix.

Table F.1: CFX setup.

Basic settings	Fluids		Air
			Water
	Reference pressure		1 atm
	Buoyancy model		Yes, -g in y-direction
		Buoyancy ref. density	1.185 [kgm3]
Fluid models	Multiphase	Homogeneous	Free surface
	Heat transfer	Homogeneous	Isothermal
	Turbulence		SST
		Wall functions	Automatic
		Buoyancy turbulence	No
Fluid specific models	Fluid buoyancy model		Density difference
Fluid pair models	Surface tension model		No
	Interphase transfer		No
	Mass transfer		No

Table F.2: CFX Solver steady state setup.

Advection scheme		High resolution
Turbulence numerics		First order
Convergence controll	Min. iterations	200
	Max. iterations	1000
Convergence criteria	Residual type	RMS
	Residual target	10^{-4}
Equation class		Continuity
		Momentum
		Turb. kin. energy
		Turb. eddy freq.
		Volume fraction

Table F.3: CFX Solver transient setup.

Advection scheme		High resolution
Transient scheme		Second order backward Euler
	Timestep initialization	Automatic
Turbulence numerics		First order
Convergence controll	Min. coeff. loops	1
		15
Time duration	Total time	0.4
Time steps	Size	0.001
Convergence criteria		10^{-4}

Table F.4: CFX Solver BC setup.

Boundary	Option	Value
Air inlet	Normal speed	30, 50 and 70
	Volume fractions	1, air
		0, water
Water inlet	Normal speed	10
	Volume fractions	0, air
		1, water
Walls	No slip walls	Smooth walls
Air outlet	Opening, relative pressure	0 Pa
	Direction	Normal to boundary
	Turbulence intensity	Medium, 5%
	Volume fractions	1, air
		0, water
Water outlet	Opening, relative pressure	0 Pa
	Direction	Normal to boundary
	Turbulence intensity	Medium, 5%
	Volume fractions	0, air
		1, water

G   CFD results

Results from the other simulation cases are presented here.

10° angle of attack

$U_{inlet} = 30m/s$, two-phase

Velocity profile at the inlet section ($x = -0.15$)is given in figure G.1.
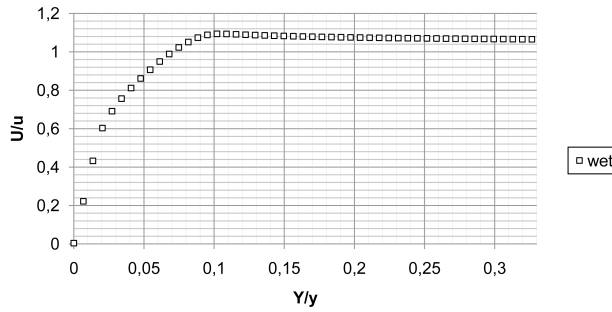
Figure G.1: Velocity profile for $U_{inlet} = 30m/s$. Normalized with inlet velocity and height of inlet section.

Shear strain rate profile at the inlet section ($x = -0.15$) is given in figure G.2.
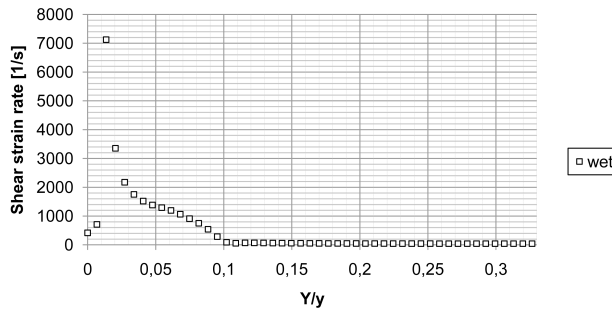
Figure G.2: Shear strain rate profile for $U_{inlet} = 30m/s$, inlet section. Normalized with the height of inlet section.

Shear strain rate profile at the profile section ($x = 0.14$) is given in figure G.3.
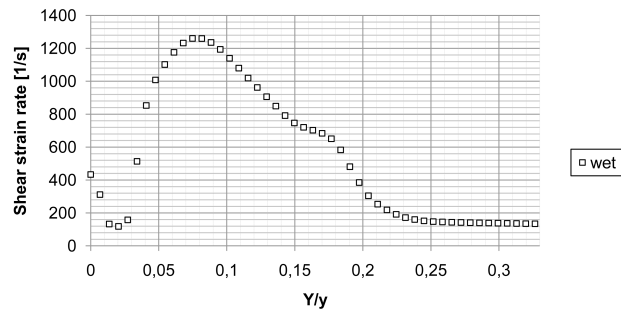
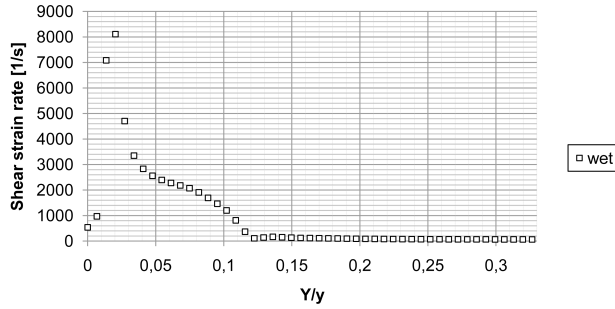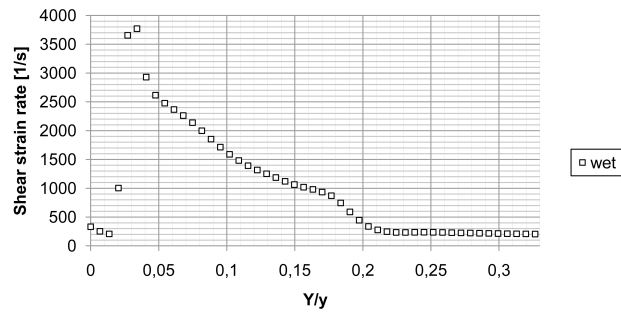**Figure G.3:** Shear strain rate profile for $U_{inlet} = 30m/s$, profile section

$U_{inlet} = 50m/s$, **two-phase**

Velocity profile at the inlet section $(x = -0.15)$is given in figure G.4.
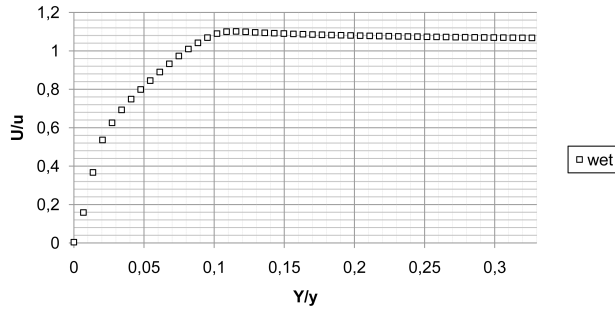
Figure G.4: Velocity profile for $U_{inlet} = 50m/s$. Normalized with inlet velocity and height of inlet section.

Shear strain rate profile at the inlet section $(x = -0.15)$ is given in figure G.5.
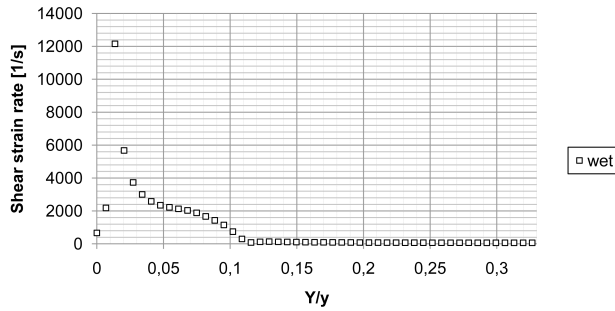
Figure G.5: Shear strain rate profile for $U_{inlet} = 50m/s$, inlet section. Normalized with the height of inlet section.

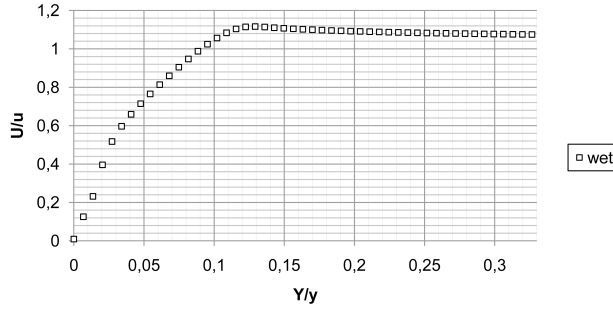Shear strain rate profile at the profile section ($x = 0.14$) is given in figure G.6.
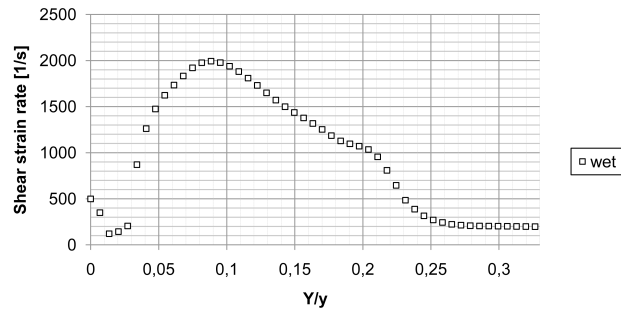
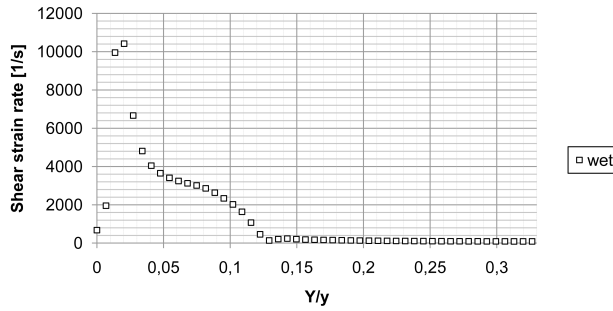**Figure G.6:** Shear strain rate profile for $U_{inlet} = 50m/s$, profile section

5° angle of attack

$U_{inlet} = 30m/s$, **two-phase**

Velocity profile at the inlet section $(x = -0.15)$is given in figure G.7.
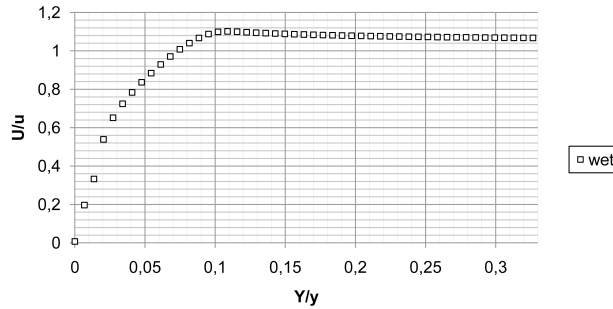
Figure G.7: Velocity profile for $U_{inlet} = 30m/s$. Normalized with inlet velocity and height of inlet section.

Shear strain rate profile at the inlet section $(x = -0.15)$ is given in figure G.8.
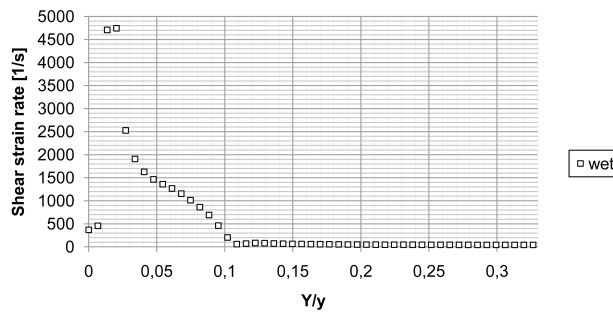
Figure G.8: Shear strain rate profile for $U_{inlet} = 30m/s$, inlet section. Normalized with the height of inlet section.

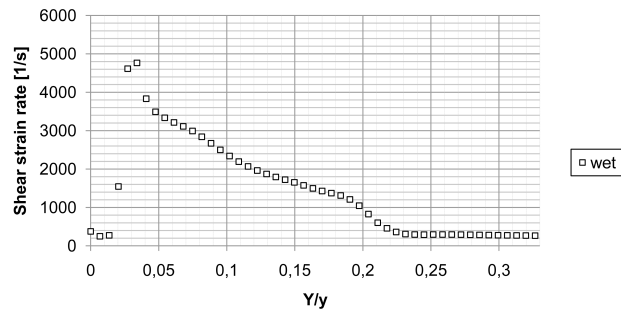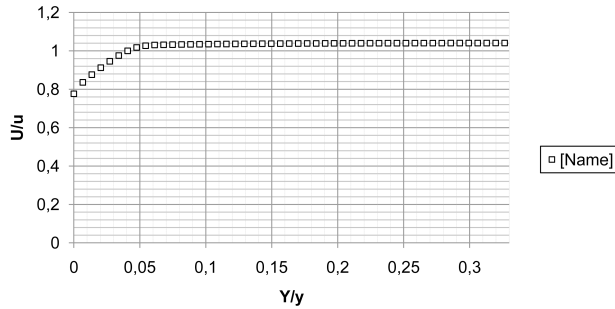Shear strain rate profile at the profile section ($x = 0.14$) is given in figure G.9.
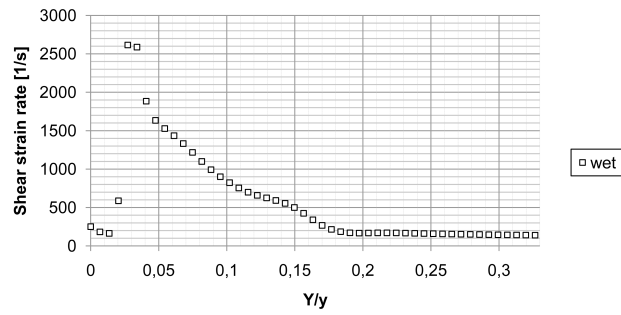
Figure G.9: Shear strain rate profile for $U_{inlet} = 30m/s$, profile section
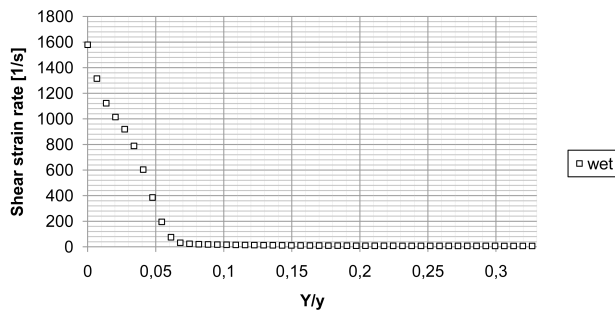
$U_{inlet} = 50m/s$, **two-phase**

Velocity profile at the inlet section $(x = -0.15)$is given in figure G.10.
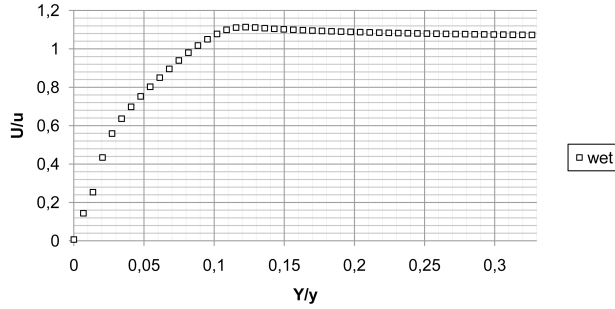
Figure G.10: Velocity profile for $U_{inlet} = 50m/s$. Normalized with inlet velocity and height of inlet section.

Shear strain rate profile at the inlet section $(x = -0.15)$ is given in figure G.11.

Figure G.11: Shear strain rate profile for $U_{inlet} = 50m/s$, inlet section. Normalized with the height of inlet section.

Shear strain rate profile at the profile section ($x = 0.14$) is given in figure G.12.

Figure G.12: Shear strain rate profile for $U_{inlet} = 50m/s$, profile section

$U_{inlet} = 70m/s$, **two-phase**

Velocity profile at the inlet section $(x = -0.15)$is given in figure G.13.

Figure G.13: Velocity profile for $U_{inlet} = 70m/s$. Normalized with inlet velocity and height of inlet section.

Shear strain rate profile at the inlet section $(x = -0.15)$ is given in figure G.14.

Figure G.14: Shear strain rate profile for $U_{inlet} = 70m/s$, inlet section. Normalized with the height of inlet section.

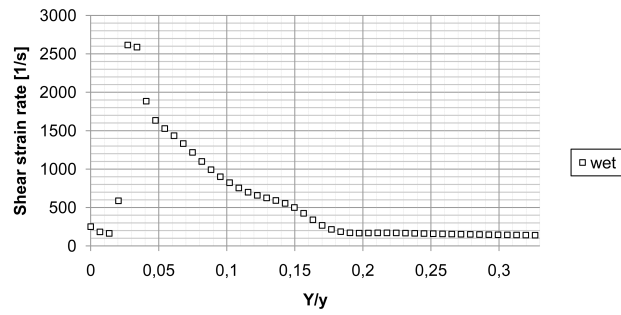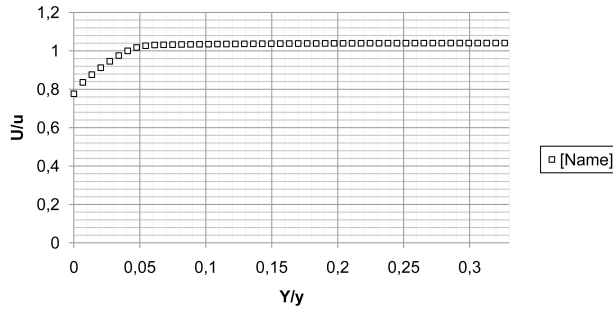Shear strain rate profile at the profile section ($x = 0.14$) is given in figure G.15.

Figure G.15: Shear strain rate profile for $U_{inlet} = 70m/s$, profile section
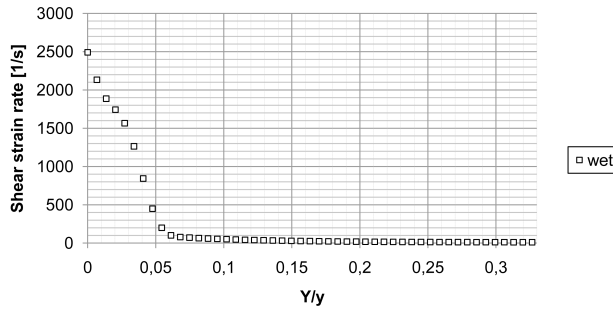
15° **angle of attack**

$U_{inlet} = 30m/s$**, two-phase**

Velocity profile at the inlet section ($x = -0.15$)is given in figure G.16.

Figure G.16: Velocity profile for $U_{inlet} = 30m/s$. Normalized with inlet velocity and height of inlet section.

Shear strain rate profile at the inlet section ($x = -0.15$) is given in figure G.17.

Figure G.17: Shear strain rate profile for $U_{inlet} = 30m/s$, inlet section. Normalized with the height of inlet section.

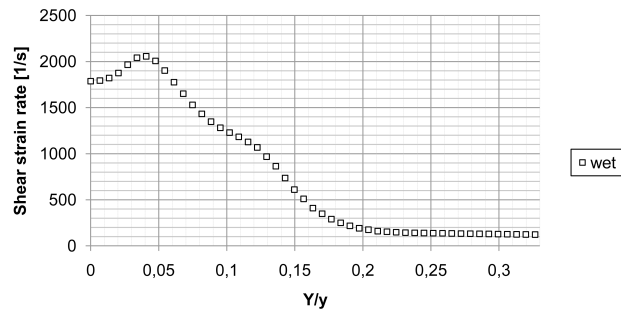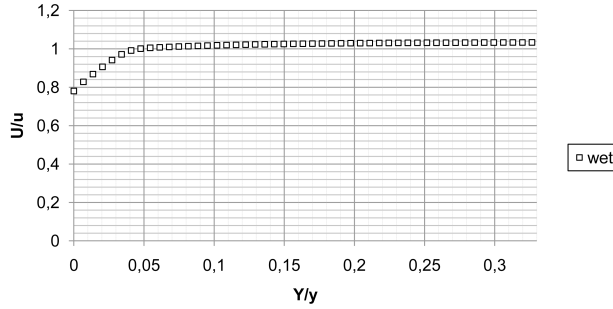Shear strain rate profile at the profile section ($x = 0.14$) is given in figure G.18.

Figure G.18: Shear strain rate profile for $U_{inlet} = 30m/s$, profile section

$U_{inlet} = 50m/s$, **two-phase**

Velocity profile at the inlet section $(x = -0.15)$is given in figure G.19.

Figure G.19: Velocity profile for $U_{inlet} = 50m/s$. Normalized with inlet velocity and height of inlet section.

Shear strain rate profile at the inlet section $(x = -0.15)$ is given in figure G.20.

Figure G.20: Shear strain rate profile for $U_{inlet} = 50m/s$, inlet section. Normalized with the height of inlet section.

Shear strain rate profile at the profile section ($x = 0.14$) is given in figure G.21.

Figure G.21: Shear strain rate profile for $U_{inlet} = 50m/s$, profile section
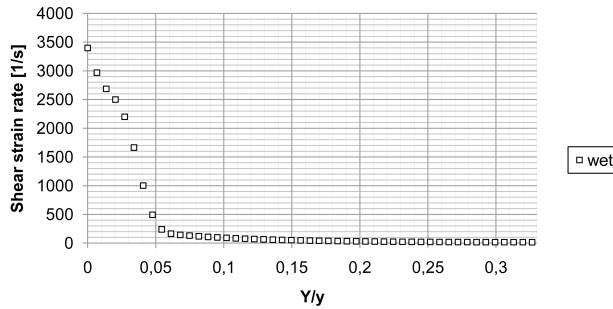
$U_{inlet} = 70m/s$, **two-phase**

Velocity profile at the inlet section $(x = -0.15)$is given in figure G.22.

Figure G.22: Velocity profile for $U_{inlet} = 70m/s$. Normalized with inlet velocity and height of inlet section.

Shear strain rate profile at the inlet section $(x = -0.15)$ is given in figure G.23.

Figure G.23: Shear strain rate profile for $U_{inlet} = 70m/s$, inlet section. Normalized with the height of inlet section.

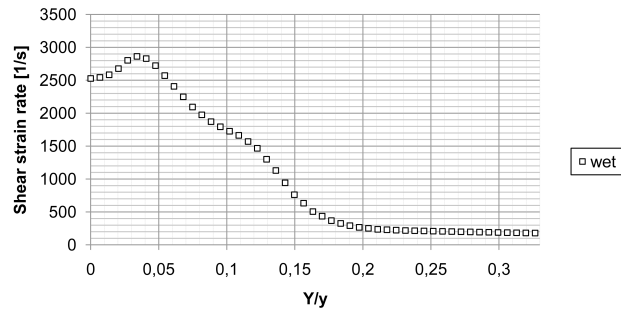Shear strain rate profile at the profile section ($x = 0.14$) is given in figure G.24.

Figure G.24: Shear strain rate profile for $U_{inlet} = 70m/s$, profile section

H   Test matrix

Next page consists of the test matrix used in the experiments.

Test procedure   m_dot=   Date:

Angle = 5 deg

Velocity [m/s]	Observations
30	
(Q=0,18)	
50	
(Q=0,3)	
70	
(Q=0,42)	

Angle = 10 deg

Velocity [m/s]	Observations
30	
(Q=0,18)	
50	
(Q=0,3)	
70	
(Q=0,42)	

Angle = 15 deg

Velocity [m/s]	Observations
30	
(Q=0,18)	
50	
(Q=0,3)	
70	
(Q=0,42)	

Other observations:

I   High speed camera data sheet

The Fastcam 1024 PCI data sheet is shown on the following two pages.

FASTCAM 1024PCI

MEGA PIXEL PERFORMANCE FOR THE PERSONAL COMPUTER

Mega pixel resolution at 1,000 frames per second for the personal computer

The FASTCAM 1024PCI from Photron is the only PC based high speed imaging system to provide 1,000 frames per second (fps) recording at full mega pixel image resolution.

Utilizing the same super light sensitive 10-bit ADC sensor as the Emmy award winning ultima APX with large seventeen microns (17µm) square pixels, the FASTCAM 1024PCI operates from 60 to 1,000 fps at full 1,024 x 1,024-pixels resolution, and at reduced resolution all the way to a top speed of 109,500 fps.

A global electronic shutter, operating down to 1.5 microseconds ensures even the fastest moving objects are frozen, blur free, in every image. Short inter-frame times make the FASTCAM 1024PCI ideal for Particle Image Velocimetry (PIV) and Digital Image Correlation (DIC) applications.

A user selectable 'Region of Interest' function enables the active image area to be windowed in steps of 128 pixels wide by 16 pixels high to allow the most efficient use of frame rate, image resolution and memory capacity for any event.

Up to 20 commonly used resolution/speed configurations can be saved to memory for future operation. A single flexible sixteen foot (5 meter) cable allows the lightweight camera head easy access to any location.

Benefits

- Variable speed resolutions, including:
  - 1,024 x 1,024-pixels at 1,000 fps
  - 512 x 512-pixels at 3,000 fps
  - 128 x 128-pixels at 27,000 fps
  - 109,500 fps at reduced resolution
- Global shuttering to 1.5µs, independent of frame rate selected
- Expandable memory offers several different configurations (PCI card and memory daughter PCB still fit in a single PCI slot) providing a wide range of record times:
  - 2GB for 1.54 seconds at 1,000 fps full resolution
  - 4GB for 3.2 seconds at 1,000 fps full resolution
  - 8GB for 6.4 seconds at 1,000 fps full resolution
  - 12GB for 9.6 seconds at 1,000 fps full resolution

Target applications include:

- Biomechanics
- 3D motion analysis
- Airbag activation analysis
- Particle Image Velocimetry (PIV)
- Digital Image Correlation (DIC)

Photron
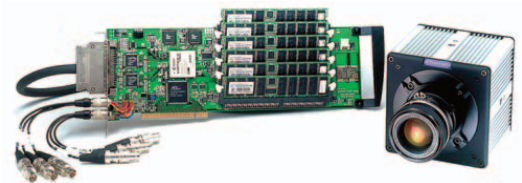
FASTCAM 1024PCI

- Biomechanics
- Microscopy
- Particle Image Velocimetry (PIV)
- Digital Image Correlation (DIC)

Specifcations

FRAME RATE (fps)	MAX RESOLUTION Horizontal	Vertical	RECORD TIME (sec) 2GB	4GB	8GB	12GB	RECORD TIME (frames) 2GB	4GB	8GB	12GB
1,000	1,024	1,024	1.54	3.2	6.4	9.6	1,536	3,200	6,400	9,600
2,000	1,024	512	1.6	3.2	6.4	9.6	3,200	6,400	12,800	19,200
3,000	512	512	2.13	4.35	8.7	13.06	6,400	13,056	26,112	39,168
6,000	512	256	2.13	4.35	8.7	13.06	12,800	26,112	52,224	78,336
10,000	256	256	2.61	5.22	10.44	15.67	26,112	52,224	104,448	156,672
18,000	256	128	2.9	5.8	11.61	17.41	52,224	104,448	208,896	313,344
27,000	128	128	3.87	7.74	15.47	23.21	104,448	208,896	417,792	626,688
45,000	128	64	4.64	9.28	18.57	27.85	208,896	417,792	835,584	1,253,376
73,000	128	32	5.72	11.45	22.89	34.34	417,792	835,584	1,671,168	2,506,752
109,500	128	16	7.63	15.26	30.52	45.79	835,584	1,671,168	3,342,336	5,013,504

Sensor 10-bit ADC (Bayer system color, single sensor) with 17μm pixel, with dual-slope over exposure protection.

Saved Image Formats AVI, JPEG, PNG, TIFF, FTIF, BMP, RAW, RAWW and Bayer. Images can be saved with or without image or comment data

Extended Dynamic Range Selectable from 4 presets to prevent over exposure

Phase Lock Enables cameras to be synchronized precisely together to a master camera or external source using the provided interconnection cables

Triggering Selectable positive or negative TTL 5Vp-p, switch closure

Lens Mount Interchangeable F-mount and C-mount standard

Dual Speed Recording™ Two-stage trigger enables the recording speed to be changed, up or down, by a factor of 2, 4 or 8 during a recording

Recording Modes Start, End, Center, Manual, Random, Random Reset, Random Center, Random Manual, and Dual Speed Recording™

Partitioning Up to 24 memory partitions are available, dependent on the memory capacity of camera

Camera Control PCI bus in a Windows PC

Software Includes image rotation and ability to save images with or without time codes or comment data

Dimensions and Weight Camera Head: 120mm (4.72")H x 120mm (4.72")W x 113.4mm (4.46")D *excluding protrusions Weight: 3.46 lbs (1.57 kg)

PCI Board: 106mm (4.17")H x 312mm (12.28")W x 1.6mm (0.06")D *Full Size PCI compliant Weight: 0.65lbs (295g) *excluding memory

Photron

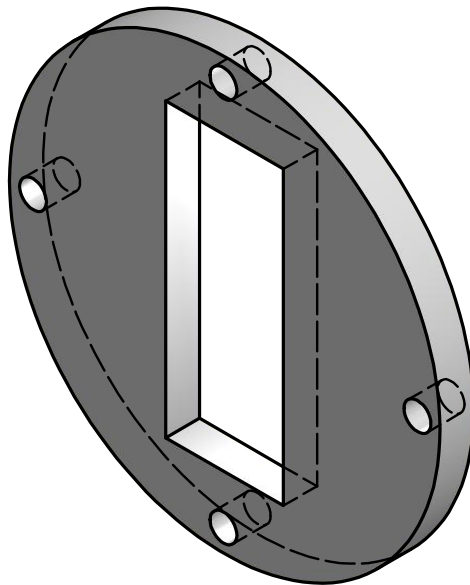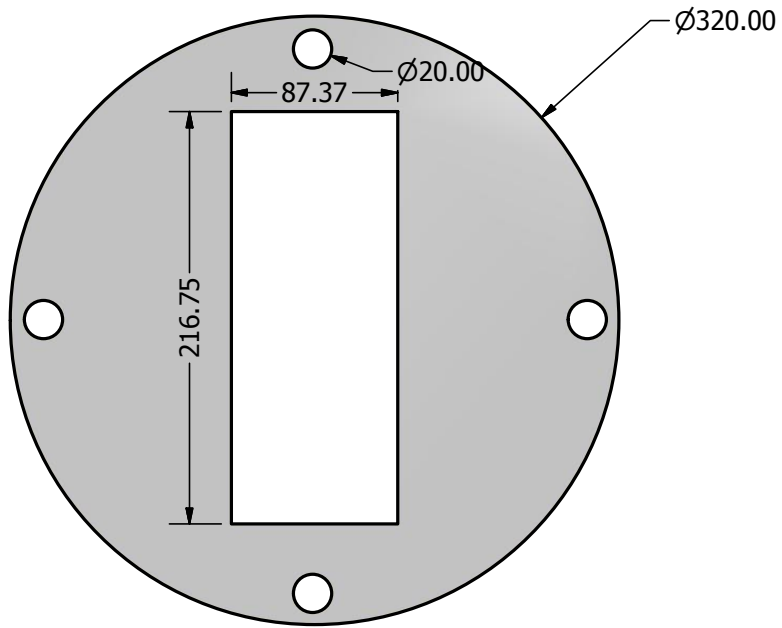SLOW MOTION IMAGING SOLUTIONS

J Technical drawings of channel

This appendix includes technical drawings made with the CAD software Autodesk Inventor Professional during the design process of the test channel.

Inlet compressor, 250Ø

Kistler dynamic pressure sensor

950.00

650.00

Inlet section

Outlet section

Water injection

Inlet channel

Lattice

Internal dimensions:
Height = 150
Width = 40

Internal dimensions:
Height = 200
Width = 40

DRAWN							
Larsen	02.06.2011						
CHECKED							
QA		TITLE					
MFG			Channel				
APPROVED							
		SIZE		DWG NO			REV
		A4		kanaldrawing			
		SCALE				SHEET 2 OF 4	

Ø320.00

Ø20.00

87.37

216.75

DRAWN			TITLE			
Larsen	02.06.2011					
CHECKED						
QA			**Transition flange**			
MFG						
APPROVED						
			SIZE	DWG NO		REV
			A4	kanaldrawing		
			SCALE		SHEET 1 OF 4	

1 mm

DRAWN			
Larsen	02.06.2011		
CHECKED			
QA			
MFG			
APPROVED			

TITLE

Water injection module

SIZE		DWG NO	REV
A4		kanaldrawing	
SCALE		SHEET 4 OF 4	

24.06

138.92

DRAWN		
Larsen	02.06.2011	
CHECKED		
QA		
MFG		
APPROVED		

TITLE

Profile

SIZE		DWG NO		REV
A4		kanaldrawing		
SCALE			SHEET 5 OF 5	